

ABSTRACT

TONG, NINGJUN. Stretchable Graphene/Hytrel[®] Electronics for Sensing and Supercapacitors. (Under the direction of Dr. Wei Gao)

The rapid development of wearable electronics has led to a fast-growing demand for pliable sensors and energy-storage units that can be seamlessly incorporated onto wearable substrates. Smart fabric sensors (SFSs), which are fabrics imbued with sensing properties, have appeared and developed rapidly in recent years due to the ubiquitous nature of fabrics. The wearable strain sensor is one of them, which can detect much higher strain compared to traditional strain sensors.

To supply energy for wearable electronics, different power units are available, such as solar cells, lithium ion batteries, and flexible thin-film batteries. However, most of them cannot meet the requirement for wearable applications, including light weight, small volume, and stability against bending, stretching and laundering. Recently, in-plane supercapacitors with the high-power density, structural flexibility, and long cycle life, are gaining increased interest from the research community.

This research is focused on developing graphene/Hytrel[®] hybrid fabrics for the strain sensing and energy storage. Our strain sensors can detect low strain (<10%) with a gauge factor of 15.2 and high strain (15 to 40%) with a gauge factor of 8.2, which are within the range of typical strain sensors. On the other hand, the supercapacitors created on our hybrid fabrics in sandwich geometry hold an average areal capacitance of $\sim 1.6 \text{ mF/cm}^2$ upon 10% strain. When in-plane concentric circular geometry was chosen for our supercapacitors, an areal capacitance of 0.78 mF/cm^2 was obtained.

© Copyright 2017 Ningjun Tong

All Rights Reserved

Stretchable Graphene/Hytrel[®] Electronics for Sensing and Supercapacitors

by
Ningjun Tong

A thesis submitted to the Graduate Faculty of
North Carolina State University
in partial fulfillment of the
requirements for the degree of
Master of Science

Textile Engineering

Raleigh, North Carolina

2017

APPROVED BY:

Dr. Wei Gao
Chair of Advisory Committee

Dr. Samuel M. Hudson

Dr. Minyoung Suh

BIOGRAPHY

Ningjun Tong was born and raised in Wuhu, Anhui, China in 1993. He received his bachelor degree in Textile Engineering in Jiangnan University in June 2016. He was admitted to the College of Textiles, North Carolina State University as a 3+X student in August 2015, and he became a master student in Textile Engineering in August 2016.

ACKNOWLEDGMENTS

First and foremost, I would like to thank Dr. Gao and my team members, Nanfei He, Qin Pan and Yixin Liu, who helped me a lot in my thesis research. I would like to take Dr. Shim, she gave me a lot of guidance during the experiments. Also thanks to Dr. Hudson and Dr. Suh for being my committee members and responsible for my research.

Secondly, I would give my sincere appreciation to all those who helped me work out my problems in study and life, they gave me their help and time without any complaint. Last my deepest gratitude goes to my beloved parents and family for their loving considerations and constant confidence in me all through these years.

TABLE OF CONTENTS

LIST OF TABLES	vi
LIST OF FIGURES	vii
CHAPTER 1 Introduction	1
1.1 Background	1
1.2 Objective	2
CHAPTER 2 Literature Review	3
2.1 Introduction of Graphene	3
2.1.1 Synthesis of Graphene <i>via</i> Graphene Oxide.....	4
2.1.2 Properties of Graphene	8
2.2 Introduction of Wearable Sensors	9
2.2.1 Flexible Strain Sensors	11
2.2.2 Strain-Responsive Mechanisms.....	13
2.3 Introduction of Supercapacitors	15
2.3.1 Energy Storage Mechanisms	17
2.3.2 Electrochemical Characterizations	20
CHAPTER 3 Experiments	22
3.1 Hytrel [®] Material	22
3.2 Experimental Procedure	24
3.3 Characterization Methods	28
3.3.1 Mechanical Test.....	28
3.3.2 Resistance Test	29

3.3.3 Electrochemical Test	30
CHAPTER 4 Results and Discussion	32
4.1 Mechanical Properties of Hytrel®	32
4.1.1 Stretchiness.....	32
4.1.2 Cycling Property.....	34
4.2 Strain Sensor Performances	35
4.2.1 Resistance Change Under Strain	35
4.2.2 Heart Rate Detection	38
4.2.3 Prototype of Strain Sensor.....	39
4.3 Supercapacitor Performances	41
4.3.1 Stretchable Sandwich Supercapacitors.....	41
4.3.2 In-plane Concentric Circular Supercapacitors.....	45
CHAPTER 5 Conclusions and Future work	48
5.1 Conclusions	48
5.2 Future Work	49
REFERENCES.....	50
APPENDICES	56

LIST OF TABLES

Table 2.1 Comparison of common reduction methods [18]	7
Table 2.2 Property values of graphene [6, 12, 24]	8
Table 2.3 Summary of performances of resistive strain sensors [36, 37]	12
Table 2.4 Comparison of properties of batteries, electrostatic capacitors and supercapacitors [43] ...	16
Table 3.1 Property values of Hytrel [®] RS 40F3 NC010	23
Table 3.2 Four samples of Hytrel [®] RS 40F3	24
Table 4.1 Hytrel [®] stretchiness test data	32
Table 4.2 The average fabric stretch and growth of Hytrel [®]	33
Table 4.3 Fabric deformation after stretching 10 cycles at different strain	34
Table 4.4 The average fabric growth of coated RS1 after 10 cycles at 40% strain	35
Table 4.5 The areal capacitance and its change upon stretching	41
Table 4.6 The areal capacitance and its change of the supercapacitor S3	43
Table 4.7 The areal capacitance of supercapacitor C1, C2 & C3	46

LIST OF FIGURES

Figure 2.1 Schematic diagram of carbon nanostructures [11]	4
Figure 2.2 Illustration of different graphene synthesis methods [12]	5
Figure 2.3 Lerf-Klinowski model of GO sheet [16, 17]	6
Figure 2.4 Illustration of the remote health monitoring system based on wearable sensors [29]	10
Figure 2.5 Schematic illustration of graphene slippage under different strains [39]	14
Figure 2.6 A series of optical images and corresponding schematics showing crack origination and propagation under different strain [2]	15
Figure 2.7 Schematic diagram of a supercapacitor cell [46]	17
Figure 2.8 Schematics for (a) an all carbon EDLC, (b) a pseudocapacitor (MnO ₂ depicted center) [47]	18
Figure 3.1 Polymer chain structure of Hytrel [®]	22
Figure 3.2 Uncoated, coated and reduce GO/Hytrel [®] samples	27
Figure 3.3 The schematics and actual devices of two supercapacitor configurations	28
Figure 3.4 Initial resistance and increased resistance upon stretching of the rGO/Hytrel [®] film	30
Figure 3.5 Two supercapacitor device assemblies including in-plane and sandwich geometries	31
Figure 4.1 The average fabric growth after 10 cycles at different strain	34
Figure 4.2 The resistance change and gauge factor under low strain for 10 cycles, a & b for sample 1; c & d for sample 2	36
Figure 4.3 The resistance change and gauge factor under the strain for 5 cycles, a & b for sample 1; c & d for sample 2	37
Figure 4.4 The voltage vs. time curve for heart rate detection	38
Figure 4.5 The circuit schematic and prototype of strain sensor	39
Figure 4.6 The CV curves of supercapacitors S1 and S2	42

Figure 4.7 The areal capacitance of S3 during stretching cycles	43
Figure 4.8 The CV curves of S3 with different scan rates	44
Figure 4.9 Nyquist plots of supercapacitor S1& S2. (Right insets) Zoom-in images of the high- frequency regime	45
Figure 4.10 The CV and Nyquist plots of supercapacitor C1, C2 & C3, the same sample of each row. (Right insets) Zoom-in images of the high-frequency regime of Nyquist plots	47

CHAPTER 1 INTRODUCTION

1.1 Background

Due to the rapid development of wearable electronics, stretchable conductive materials (SCMs) have attracted more and more interest for portable and wearable system, since they bare unique features that are key in relevant applications, such as large strain endurance, exceptional electrochemical stability upon repeated deformations, *etc.*

Strain sensors measure local deformations. Traditional sensors (made of semiconductors or meta) usually have high sensitivities and low cost. However, most of them are fixed directional sensors and strain can only be measured in a specific direction, moreover, they can only detect low strains due to the limited stretchability. Sensors based on nanomaterials (e.g. nanoparticles, nanotubes, and thin films) exhibit excellent characteristics including a high elastic moduli and outstanding electrical properties when compared to the traditional sensors [1-3]. In terms of graphene-based sensors, its topological structure can be modulated by applying uniaxial strain, which will affect the principal vibrational frequencies and electrical conductance of graphene, thus can be used for high sensitivity strain sensing.

Most of wearable electronics need energy sources, and electrochemical energy storage devices can be integrated together with textile to achieve fully power-independent and stretchable systems. Supercapacitors are ideal alternative energy storage devices with high power supply and long cycle life, which bridge the power or energy gap between traditional electrostatic capacitors and batteries by storage more energy than the former as well as delivering higher power than the latter, respectively. Stretchable supercapacitors can accommodate high strain while offering electrical energy for other devices in the circuits [4,

5]. Graphene-based electrodes have been made into supercapacitors with relative simple fabrication processes and low cost, which have demonstrated excellent electrochemical performances.

1.2 Objective

In response to the wearable electronics in smart textiles, we will incorporate two types of functional components onto stretchable fabrics (Hytrel[®]): 1) strain sensors based on electrical conductivity of surface coatings with graphene, to sense against local deformations; 2) energy storage units based on graphene oxide coating and laser-patterning processes on fabric surfaces that can sustain certain levels of stretching/twisting.

For the graphene-based strain sensors, a thin-layer of graphene flakes ($\sim 1 \mu\text{m}^2$ in size on average) will be coated onto the Hytrel[®] sample surface, and the resistance of the surface coating will be monitored upon external stretching. We will also explore the factors that can influence the sensitivity of strain sensors to optimize it. As for the stretchable graphene-based supercapacitors, different structures (sandwich and in-plane concentric circular geometries) of electrodes will be created *via* laser-patterning processes to compare the capacitance density and stretchiness.

CHAPTER 2 LITERATURE REVIEW

2.1 Introduction of Graphene

Graphene, one of the allotropes (carbon nanotube, fullerene, diamond) of elemental carbon, is a one-atom-thick planar sheet of sp^2 -bonded carbon atoms densely packed in a two-dimensional (2D) honeycomb crystal lattice [6-8].

Although the use of naturally occurring graphite started 6000 years ago, graphene, the building block of graphite, was theoretically established in 1940 [9]. The research of graphene had grown slowly in the late 20th century, since graphene preparation was considered to be a formidable task experimentally due to the conventional perception that the single-layer graphene was thermodynamically unstable in real state [7, 8]. Various attempts had been made to synthesize graphene, yet, it was until 2004 that Prof. Andre Geim and Dr. Konstantin Novoselov at Manchester University successfully obtained the first piece of graphene by mechanical exfoliation HOPG (highly oriented pyrolytic graphite) with adhesive tapes [10]. They were awarded with the Nobel Prize in Physics in 2010 “for ground breaking experiments regarding the two-dimensional material graphene”. Since its discovery in 2004, publications on graphene blossomed.

Graphene is the basic building block of all the other allotropes of carbon. As shown in Figure 2.1, graphene, is just a single atomic layer of covalently connected sp^2 carbon atoms arranged in a hexagonal honeycomb lattice. It can be either wrapped up to form 0D fullerenes, or rolled up with respect to its axis to form 1D carbon nanotubes (CNTs), or stacked up to yield 3D bulk graphite *via* the weak van der Waals force [6, 8, 11].

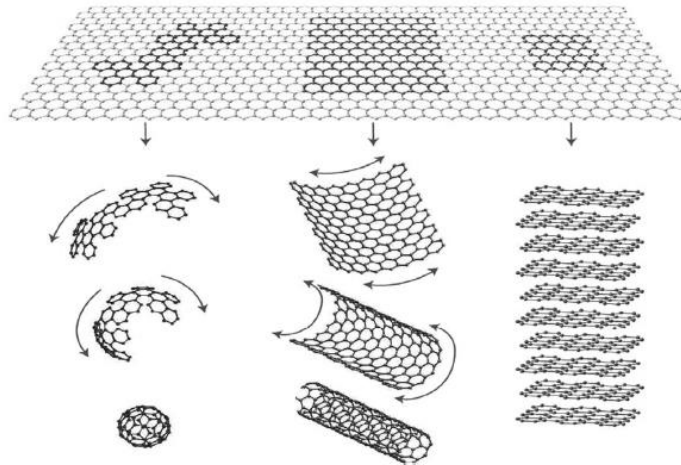


Figure 2.1 Schematic diagram of carbon nanostructures [11].

2.1.1 Synthesis of Graphene *via* Graphene Oxide

To date, there are several techniques developed to prepare graphene in various sizes, shapes and qualities. An overview of graphene synthesis strategies is shown in Figure 2.2, which can be classified as “top-down” methods including mechanical exfoliation, chemical exfoliation and synthesis, as well as “bottom-up” techniques, including pyrolysis, epitaxial growth and chemical vapor deposition (CVD) [7, 11-14]. Among them, mechanical exfoliation, CVD, chemical exfoliation and chemical synthesis *via* graphene oxide are most commonly used today and might be commercially available in the future [12, 13]. Here we adopt the chemical synthesis *via* graphene oxide as discussed below.

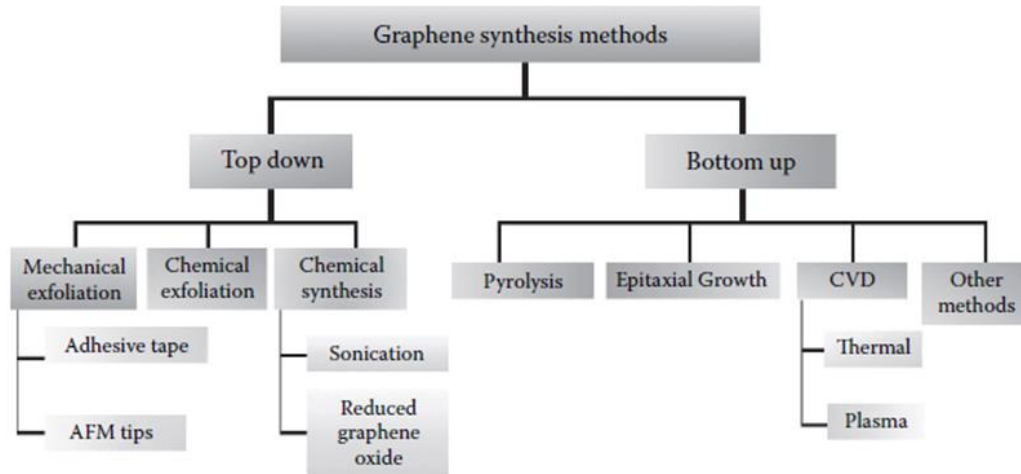


Figure 2.2 Illustration of different graphene synthesis methods [12].

The chemical synthesis of graphene *via* graphene oxide (GO) involves the chemical oxidation of graphite powders, dispersion of GO in aqueous solutions and reduction of GO back to graphene. Three popular methods are currently used for the GO synthesis, Brodie method, Staudenmaier method, and Hummers method [12]. Based on the modified Hummers method, GO is prepared through the oxidation of graphite using strong acids and oxidants including sulfuric acid (H₂SO₄), sodium nitrite (NaNO₂) and potassium permanganate (KMnO₄) [15]. When graphite turns into GO, the interlayer spacing will increase two or three times than in pristine graphite, which can easily distinguish a single layer from the bulk materials. Besides, GO is heavily oxygenated, its hydroxyl and epoxy groups are located on sp³ hybridized carbon on the basal plane, and carbonyl and carboxyl groups are located on sp² hybridized carbon at the sheet edges [7]. Therefore, GO is highly hydrophilic and readily exfoliated in water to form a stable colloidal system, it consists mostly of single layered sheets without the assistance of surfactants due to its hydrophilicity and electrostatic repulsion, and

its acknowledged model proposed by Lerf and Klinowski is presented in Figure 2.3, which is nonstoichiometric [16, 17].

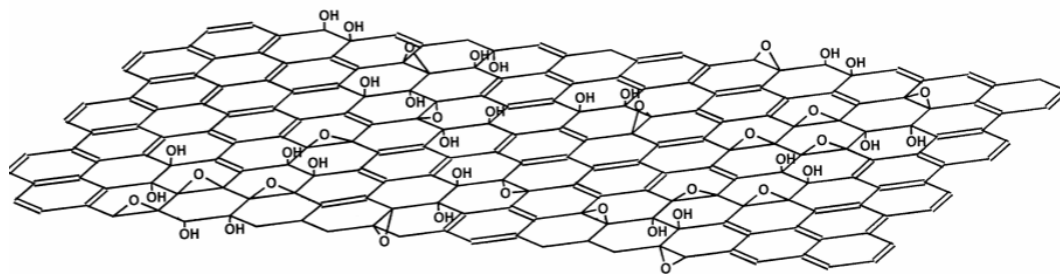


Figure 2.3 Lerf-Klinowski model of GO sheet [16, 17].

The oxygen-containing functional groups of GO provide many reactive sites for various surface-modification reactions to develop different graphene-based materials. On the other hand, these functional groups also disrupt the electronic structure, in addition to irreversible defects and disorders, which results in diminished electrical conductivity in GO [7]. So many approaches to remove oxygen-containing groups and heal structural defects appeared, including chemical, thermal, laser-scribe and electromagnetic flash methods. A comparison of common reduction methods is shown in Table 2.1 [6-8, 18-23]. Among them, chemical reduction of GO sheets is commonly used for electrochemistry applications. Chemical reduction by solutions or vapor of reducing agents has been demonstrated with hydrazine (N_2H_4), sodium borohydride ($NaBH_4$), hydroiodic acid (HI), ascorbic acid (Vc), and strong alkali solutions (KOH, NaOH), *etc.* at room temperature or with moderate heating [18, 19]. Another chemical method is solvothermal reduction. In a sealed container, overheated supercritical (SC) water is used as the reaction media, offering a green alternative to organic solvents [20]. Besides, GO can also be reduced *via* electrochemical method using a normal

electrochemical cell [21] or through photo-chemical reaction in presence of a photo-catalyst such as TiO₂ under ultraviolet (UV) irradiation [22].

Table 2.1 Comparison of common reduction methods [18].

Reduction method	Form	C/O ration	σ (S/cm)
Hydrazine hydrate	Power	10.3	2
150 mM NaBH ₄ solution, 2 h	TCF ^{a)}	8.6	0.045
Hydrazine monohydrate	Film	12.5	77
Thermal annealing at 1100 °C, UHV	TCF	NA ^{b)}	~1000
Thermal annealing at 1100 °C in Ar/H ₂	TCF	NA	727
Vitamin C	Film	12.5	77
KOH	Film	NA	1.910 ⁻³
55% HI reduction	Film	>14.9	298

^{a)} TCF: transparent conductive film; ^{b)} NA: not available.

However, chemical reduction cannot fully eliminate functional groups in GO, which results in inferior products, usually named as reduced graphene oxide (rGO). This is because different reducing reagents may select specific oxygen-containing groups to react with. In general, different functional groups in GO have different binding energies to the basal planes, for instance, it is relatively easy to remove epoxy and hydroxyl groups located within the graphitic domain without lattice defects, while those located on the defective sites and edges are hard to fully remove [18]. Thus, a well-designed reduction method combining chemical reduction and moderate thermal annealing may remove most of functional groups in GO resulting in low defect concentrations [23].

Chemical synthesis of graphene *via* GO conversion has the advantages of scalable, rapid, cost effective and easy handling; however, rGO is far from perfect graphene structures, it usually has abundant structural defects and remaining functional groups, which readily deteriorates the electrical and mechanical properties as compared to other graphene samples [7, 12].

2.1.2 Properties of Graphene

Graphene is the thinnest, strongest, and stiffest known material, which is a single layer of carbon atoms bonded together with sp^2 - sp^2 bonds at the length of 0.141 nm in a 2D hexagonal lattice [8]. Graphene has demonstrated a variety of superior properties so far including high optical transparency, superior electrical and thermal conductivity, excellent mechanical properties, in addition to a low coefficient of thermal expansion (CTE) behavior [6-8, 12]. Some reported properties of graphene are presented in Table 2.2.

Table 2.2 Property values of graphene [6, 12, 24].

Properties	Details
Optical transparency	97.7%
Thermal conductivity	$5000 \text{ W} \cdot \text{m}^{-1} \cdot \text{K}^{-1}$
Electron mobility	$25\,000 \text{ cm}^2 \cdot \text{V}^{-1} \cdot \text{s}^{-1}$
Specific surface area	$2630 \text{ m}^2 \cdot \text{g}^{-1}$
Breaking strength	$42 \text{ N} \cdot \text{m}^{-1}$
Young's modulus	1.0 TPa
Stiffness	$400 \text{ N} \cdot \text{m}^{-1}$

Especially, graphene has some excellent electrochemical properties. First, it has the high specific surface area of $2630 \text{ m}^2 \cdot \text{g}^{-1}$ theoretically, which is two times larger than that of CNTs ($1315 \text{ m}^2 \cdot \text{g}^{-1}$) and much higher than that of graphite (*ca.* $10 \text{ m}^2 \cdot \text{g}^{-1}$). Moreover, the electrical conductivity of graphene has been calculated to be *ca.* $64 \text{ mS} \cdot \text{cm}^{-1}$, approximately 60 times greater than that of single-walled carbon nanotubes (SWCNTs) [24]. An ultra-high electron mobility of $> 200,000 \text{ cm}^2 \cdot \text{V}^{-1} \cdot \text{s}^{-1}$ at room temperature in suspended graphene also has been reported [25]. Such high electronic conductivity and electron mobility in graphene results from unique electronic structure of this 2D electron gas, while high crystallinity in structure is required for these fascinating properties.

However, the conductivity and electron mobility in rGO are 3 and 2 orders of magnitude lower than that of graphene, respectively [7], which result from the existing defects and lattice vacancies which cannot be healed during reduction processes. Recently, an rGO sample was prepared with the electrical conductivity of 72 S/cm at room temperature, which can be used in supercapacitors [26].

Due to these superior properties, graphene has been used in various applications including coatings, paints or inks, composites, TCF, energy storage devices, flexible sensors and organic light-emitting diodes (OLEDs) displays, *etc.*

2.2 Introduction of Wearable Sensors

Wearable sensors have become very popular in many applications such as medical, sport and entertainment fields due to their readily interaction with human body. They are created by incorporating conductive materials into textile structures, hence, they can be easily integrated into clothing or directly attached onto skin to achieve real-time and ubiquitous sensing [27].

With the recent advances in flexible electronics, more and more wearable sensors may get into our daily lives with a variety of functions, e.g. health monitoring. The physiological signals captured by these sensors, such as heart rate, respiration rate, blood pressure and skin temperature, can provide accurate and reliable information on users' physiological status with technical analysis, which helps keep users monitored during physical activities. A remote health monitoring system based on wearable sensors is presented in Figure 2.4 [28, 29]. The detected signals originate from physical and chemical sensing [30]. For the former, thermal and mechanical sensors have been applied to monitor temperature and strain changes, such as thermos-resistive sensors, piezoresistive and piezoelectric sensors. For the latter, chemical sensors or biosensors are used to detect different chemicals, e.g. toxic vapors (like nitrous oxide) and organic species in sweats.

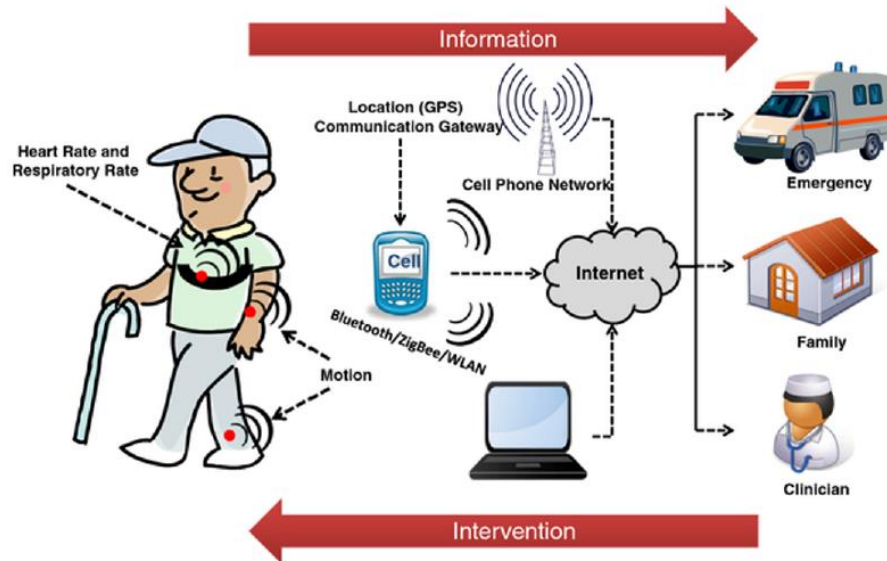


Figure 2.4 Illustration of the remote health monitoring system based on wearable sensors [29].

2.2.1 Flexible Strain Sensors

The strain sensor can measure strain or local deformations applied on an object by electrical signals, which is invented in 1938 by Edward E. Simmons and Arthur Claude Ruge independently, as one of the most important devices in the measurement of mechanical quantities [31]. The most common strain sensor is based on the electrical conductance change. When an electrical conductor is stretched within the elastic range such that it does not break or permanently deform, the electrical resistance will increase. Conversely, the resistance will decrease as it is compressed. A commonly cited figure-of-merit representing the sensitivity of strain sensors is known as the gauge factor (GF), which is defined as:

$$GF = \frac{\Delta R/R}{\Delta L/L} = \frac{\Delta R/R}{\varepsilon} \quad (1)$$

where R is the nominal resistance of the strain sensor, ΔR is the total resistance change, L is the original unstrained length, ΔL is the total change in length under strain and ε is the applied strain. Apart from resistive strain gauges, there are some other types of strain sensors, such as capacitive strain sensors depending on the capacitance change and fiber optic strain sensors based on the relative intensity of light [32, 33].

Conventional strain sensors including metal and semiconductor strain gauges are mainly used in damage detection and fatigue studies, they can be high sensitive and low cost. However, the existing commercial products are typically bonded to the surface of solid materials and can only measure the minute distance changes in a specific direction, for instance, semiconductor strain gages can only detect very low strain, less than 2% due to the rigid material with the limited stretchability [2, 31]. Strain sensors based on nanomaterials and polymers, such as

nanoparticles, nanotubes and nanowires, have been attracting interests recently due to their capability for high-strain detection [1-3, 34-37]. For example, Amjadi and his coworkers reported a silver nanowires (AgNWs)-elastomer strain sensor with tunable gauge factors in the ranges of 2 to 14 and a high stretchability up to 70% [34]. Yamada et al. fabricated a strain sensor with aligned single-walled carbon nanotube (SWCNT) thin film, which could measure high strain up to 280% and detect human motion [35]. Graphene has also been extensively studied for strain sensors owing to its extraordinary electrical and mechanical properties. Graphene was added into a lightly cross-linked silicone to obtain an electromechanical sensor at a level of precise sensitivity of gauge factor >500, and it could monitor deformation, pressure and impact, which can be used to measure pulse, blood pressure and even the impact associated with the footsteps of a small spider [1]. In addition, graphene woven fabric (GWF) thin film *via* atmospheric pressure CVD method was coated onto or embedded in polydimethylsiloxane (PDMS) matrix, the electrical resistance of strain sensors significantly increased with tensile strain with gauge factors of ~103 under 2~6% strains and ~106 under higher strains [2]. Table 2.3 presents the performances (gauge factor and strain range) of resistive strain sensors.

Table 2.3 Summary of performances of resistive strain sensors [36, 37].

Materials	Gauge factor	Strain range (%)
AgNWs-PDMS	2-14	70
Aligned SWCNTs-PDMS	0.82	280
CNTs- Ecoflex rubber	1	150
Graphene foam-PDMS	114	70
Graphene-rubber	10-35	800

2.2.2 Strain-Responsive Mechanisms

Strain sensors respond to the applied strain with different mechanisms based on materials, and fabrication processes. Here, we only focus on the mechanisms of resistive strain sensors. Strain-resistance response of traditional strain sensors results from geometrical effect and piezoresistivity of materials [31, 36]. As for the former (geometrical effect), the resistance of a conduct is given by:

$$R = \rho \frac{L}{A} \quad (2)$$

where ρ is the electrical resistivity, an intrinsic property of the conductor, and A is the cross-section area. When a material is stretched, it tends to contract in the directions transverse to the stretching based on the Poisson effect, hence, the resistance increases with the elongation in length and shrinkage in cross-sectional area when it is stretched. For the latter (piezoresistivity), the resistance change originates from electrical resistivity change due to the structural deformation of materials, the relative resistance change includes geometrical and piezoresistive effects, and it is presented as:

$$\frac{\Delta R}{R} = (1 + 2\nu)\varepsilon + \frac{\Delta\rho}{\rho} \quad (3)$$

where ν is the Poisson's ratio of the material, $\Delta\rho$ is the change of electrical resistivity. In addition to metal and semiconductor materials, nanomaterials such as CNT and zinc oxide nanowire also showed high piezoresistivity. Piezoresistive effect can increase the gauge factor (GF) of strain sensors, since it enhances the resistance change, especially for semiconductor sensors [38].

Apart from the geometrical effect and piezoresistivity in traditional strain sensors, there are other three specific mechanisms explained for the piezoresistivity change in nanomaterials: disconnection mechanism, crack propagation and tunneling effect [36]. For nanomaterial thin films, the electrical conductivity is achieved by electrons transferring through the overlapped nanomaterial network. When they are stretched, some conductive nanomaterials may slip and be disconnected from the network owing to the weak interfacial binding energy and large stiffness difference between nanomaterials and stretchable polymers, which will increase the electrical resistance of the sensors [36, 39]. Figure 2.5 presents the schematic illustration of the slippage of overlapping graphene sheets under different strains. This flexible strain sensor based on self-locked overlapping graphene sheets (SOGS) had a high GF up to 400 and strain range over 7.5%, and it could detect various human motions and human sounds.

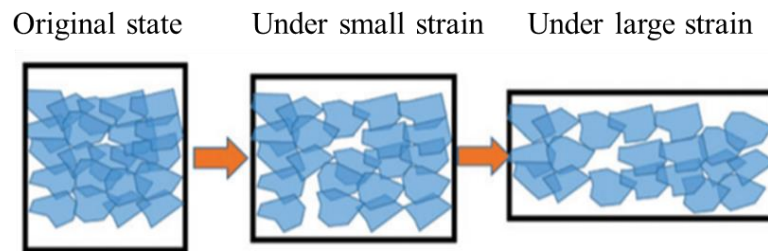


Figure 2.5 Schematic illustration of graphene slippage under different strains [39].

Crack propagation is another mechanism used in nanomaterial thin films for the resistance change, due to the brittleness of nanomaterial thin films, cracks originate and propagate in thin films upon stretching, shown in Figure 2.6, which limits the mean free path of electrons through films and increases the electrical resistance. Most GWFs-PDMS strain sensors are based on this mechanism [2, 40]. In terms of tunneling effect, it means electrons can pass through a barrier such as a thin insulating polymer layer by the process of quantum tunneling, the distance

between adjacent nanomaterials is very important. The strain sensor of AgNWs-PDMS we mentioned previously is based on the tunneling effect, its resistance can be estimated by Simmons's theory [34, 41]:

$$R_{tunnel} = \frac{V}{AJ} = \frac{h^2 d}{Ae^2 \sqrt{2m\lambda}} \exp\left(\frac{4\pi d}{h} \sqrt{2m\lambda}\right) \quad (4)$$

in which V is the electrical potential difference, A is the cross-sectional area of the tunnel, J is tunneling current density, h is Plank's constant, d is the distance between two adjacent nanomaterials, e is the quantum of electricity, m is the mass of electron, λ the height of barrier for insulating polymers.

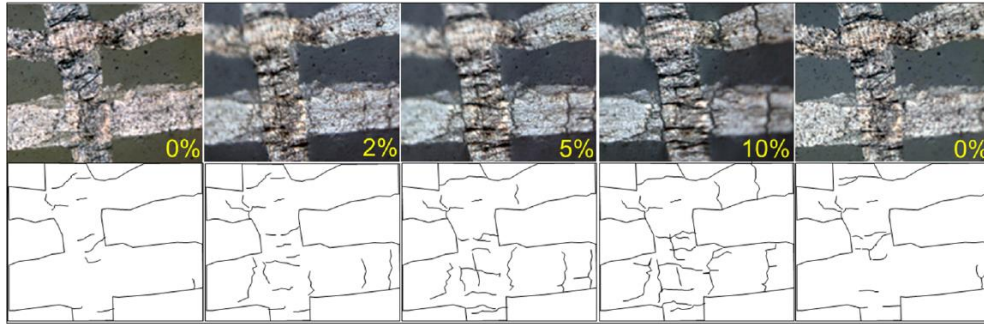


Figure 2.6 A series of optical images and corresponding schematics showing crack origination and propagation under different strain [2].

2.3 Introduction of Supercapacitors

The most common electrical-energy storage devices in our daily life are batteries, which can store a large amount of energy in a relatively small volume or weight. However, batteries also have some limitations, such as short shelf and cycle life, and low power density. Specifically, rechargeable batteries will degrade if they are unused for a long time due to self-discharge and corrosion effects [42]. In addition, with the development of electrical devices

recently, the high-power requirements have exceeded the capability of batteries of standard design. So, supercapacitors are ideal alternatives to batteries with much higher efficiency and power, as well as much longer shelf and cycle life than batteries. As shown in Table 2.4, the energy density of supercapacitors is at least 10 times higher than that of electrostatic capacitors, and supercapacitors also have much higher specific power and charge-discharge efficiency, longer cycle life and shorter discharge time compared to batteries. On the other hand, supercapacitors have relatively lower energy density than batteries, which will limit their use in some applications [43]. Thus, supercapacitors bridge the power and energy gaps between traditional electrostatic capacitors and batteries.

Table 2.4 Comparison of properties of batteries, electrostatic capacitors and supercapacitors [43].

	Batteries	Electrostatic capacitors	Supercapacitors
Discharge time	0.3-3 h	10^{-6} - 10^{-3} s	0.3-30 s
Charge time	1-5 h	10^{-6} - 10^{-3} s	0.3-30 s
Energy density (Wh/kg)	10-100	<0.1	1-10
Specific power (W/kg)	50-200	>10000	~1000
Charge-discharge efficiency	0.7-0.85	~1	0.85-0.98
Cycle life	500-2000	>500000	>100000

The earliest supercapacitor patent was filed by Becker at General Electric Corp. in 1957. However, not until 1990s did supercapacitor technology begin to attract attention due to the emergence of hybrid electric vehicles, which depended on batteries and fuel cells to provide the necessary power for acceleration and additional energy for brake recuperation [44]. Now

supercapacitors are used in many applications such as consumer electronics, and a more recent application of ECs in Airbus A380 has shown their excellent and reliable performance [45]. A conventional supercapacitor includes two electrodes and a separator sandwiched between them that are sealed in electrolyte liquids, solid-state gels or polymer electrolytes. Its configuration is presented in Figure 2.7. Supercapacitor stores charge at two interfaces between the electrode and electrolyte; when it is charged, negative ions in the electrolyte will diffuse to the positive electrode, while positive ions will diffuse to the negative electrode, creating two separate capacitive storage layers [46]. Hence, a supercapacitor cell with two electrodes can be treated as two capacitors in series, and the total capacitance (C_T) of the entire cell can be calculated as:

$$\frac{1}{C_T} = \frac{1}{C_1} + \frac{1}{C_2} \quad (5)$$

where C_1 and C_2 represent the capacitances of the positive and negative electrodes, respectively.

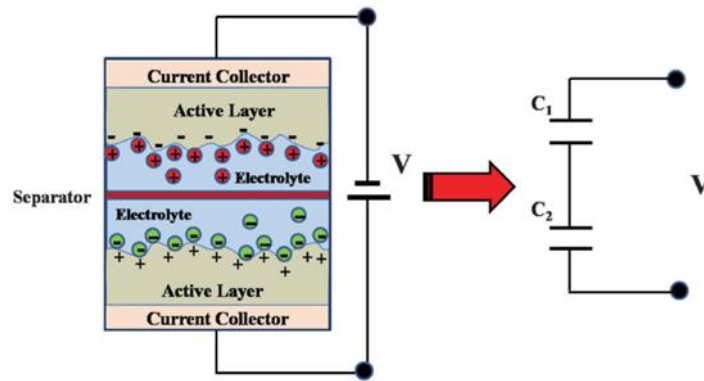


Figure 2.7 Schematic diagram of a supercapacitor cell [46].

2.3.1 Energy Storage Mechanisms

Supercapacitors store energy by charge separation depending on the different charge-storage mechanisms. They can be classified into two types: electrochemical double-layer

capacitors (EDLCs) by ion adsorption, and pseudocapacitors with fast and reversible Faradic process, as shown in Figure 2.8 [47]. These two mechanisms can function simultaneously based on the nature of the electrode material.

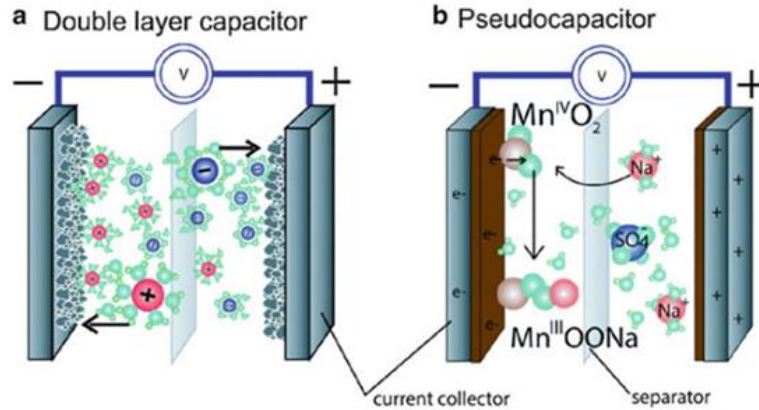


Figure 2.8 Schematics for (a) an all carbon EDLC, (b) a pseudocapacitor (MnO_2 depicted center) [47].

EDLCs store energy at the interface between the electrode and the electrolyte through the depletion of the oppositely charged species [48]. As an excess or deficiency of charge builds up on the electrode surface, ions of the opposite charge forming the double-layers in the pores are built up in the electrolyte near the interface to provide electroneutrality by diffusion through the electrolyte. In addition, the surface charge can be generated by surface dissociation, ion adsorption from solution or crystal lattice defect [43]. This is a true capacitance effect due to no charge transfer across the interface, and such accumulation of the pure electrostatic charge and electrons at the electrode is a non-Faradaic process. The specific capacitance (C) arising from an EDLC is generally analogous to a parallel plate capacitor and measured as:

$$C = \frac{A\epsilon_r\epsilon_0}{d} \quad (6)$$

where ϵ_r (a dimensionless constant) is the relative permittivity of the medium in the EDL, ϵ_0 is the permittivity of a vacuum, A is the specific surface area of the electrode accessible to the electrolyte ions, and d is the effective thickness of the EDL, depending on the concentration of the electrolyte and the size of ions.

Pseudocapacitors store energy by the redox reaction between the electrode material and the electrolyte. Underpotential deposition, redox and intercalation pseudocapacitance are three different faradaic charge storage mechanisms identified by B.E. Conway [49]. For the first one, underpotential deposition (UPD), it means the potential that metal monolayer electrodeposit on a different metal's surface is significantly less negative than the equilibrium potential for reduction of this metal, or that for deposition on the same metal surface, so the metal will deposit onto another material more easily than it deposit onto itself. Redox pseudocapacitance indicates the ion electro-adsorption onto the surface of the material occurs together with a faradaic charge transfer. Intercalation pseudocapacitance will occur when ions intercalate into the layers of the redox-active host with a concomitant charge transfer while maintaining crystallographic phase [49, 50]. The capacitance of the pseudocapacitor is voltage-dependent, since the charge transfer involving Faradaic reactions is voltage-dependent. The theoretical average capacitance (C_{av}) of a pseudocapacitor can be calculated from:

$$C_{av} = \frac{Q_T}{V_T} = \frac{nFX}{mE} \quad (7)$$

where the Q_T and V_T are the total charge and voltage change for an electrode charge/discharge, E is the potential, n is the number of electrons, F is the Faraday constant (96485 C/mol), X is the extent of fractional coverage of the (inner) structure, and m is the molecular weight of the

active material. Since the curve of E vs. X is not entirely linear, the capacitance of the capacitor is not always constant, and this is the reason why it is called pseudocapacitance.

In addition to EDLCs and pseudocapacitors discussed previously, hybrid electrochemical capacitors (HECs) are assembled with an asymmetrical configuration including one electrode of a double-layer carbon material and the other one of a pseudocapacitance material. They can achieve higher energy and power densities while keeping a good cycle stability [42]. Hybrid supercapacitors can also be fabricated by two different mixed metal oxide or doped conducting polymers. Generally, in order to improve the device performances and meet a variety of uses, many different types of supercapacitors have been developed with various electrode materials.

2.3.2 Electrochemical Characterizations

The performances of a supercapacitor are mainly evaluated based on the following aspects [45, 51]: (1) a substantially high power density greater than batteries with a relatively high energy density; (2) a high specific capacitance; (3) an excellent cycle ability more than 100 times of batteries; (4) fast charge-discharge rates within seconds; (5) low self-discharging; (6) safety, and (7) low cost. The electrochemical performances of a supercapacitor are commonly characterized by cyclic voltammetry (CV), electrochemical impedance spectroscopy (EIS) and galvanostatic charge/discharge [52]. Usually the specific capacitance can be determined from CV by integrating over the full curve or galvanostatic charge/discharge by the slope of the discharge curves. The EIS presents the frequency response of the supercapacitor system using Nyquist plots that are a plot of the imaginary impedance component (Z'') against the real one (Z'), the system corresponds more closely to an ideal capacitor when the EIS curve is more

vertical, and the equivalent series resistance (ESR) can be defined from the intersection of the curve at the X-axis, which can affect the charged/discharged rate or power capability.

Energy density (E) and power density (P) of for a single cell supercapacitor are given by, respectively [44, 45]:

$$E = \frac{C_T V^2}{2} \quad (8)$$

$$P = \frac{V^2}{4mR_s} \quad (9)$$

in which V is the potential range, C_T is the total capacitance of the cell, m is the mass of the electrode, R_s is the equivalent series resistance including the series resistances of the electrolyte and electrode, such as the intrinsic and diffusion resistance and contact resistance between the current collector and the electrode. As mentioned previously, supercapacitors have low energy density less than 10 Wh/ Kg, from both equations (8) and (9), it can be seen that increasing voltage window and capacitance or reducing ESR are able to improve the energy or power densities of the supercapacitors. For example, electrode materials should be highly electronic conductive to distribute and collect the electron current. However, the stability should be considered when reaching a high voltage which is related to on electrode materials and structures.

CHAPTER 3 EXPERIMENTS

3.1 Hytrel® Material

Hytrel®, a trademarked product of DuPont Company, is a polyether-ester block copolymer combining a hard (crystalline) segment of polybutylene terephthalate and a soft (amorphous) segment based on polyether chemistry, the polymer chain structure is presented in Figure 3.1. Hytrel® is identified as TPC-ET (thermoplastic polyester elastomer) according to ISO 1043, and it offers many of the most desirable characteristics of high-performance elastomers and plastics, such as the flexibility of rubber, the strength and processability of thermoplastics [53].

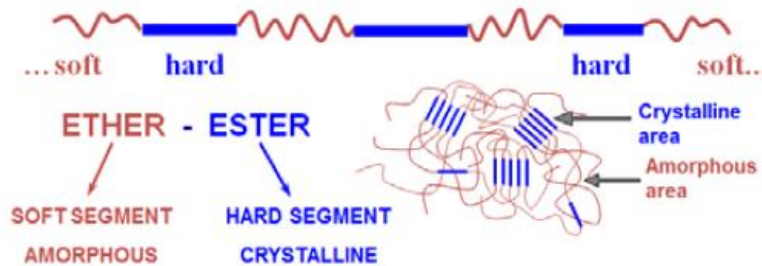


Figure 3.1 Polymer chain structure of Hytrel®.

Common features of Hytrel® thermoplastic polyester elastomer includes mechanical and physical properties, e.g. exceptional toughness and resilience, flexibility at low temperatures and good retention of properties at elevated temperatures, high resistance to creep, impact and flex fatigue. In addition, Hytrel® also resists deterioration from many industrial chemicals, oils, and solvents due to the plasticizer free, it is resistant to the same classes of chemicals and fluids, as are polyurethanes, which are both ester and ether based, but has better high-temperature properties than the polyurethanes and can be used satisfactorily at higher temperatures in the

same fluids. Hytrel[®] has excellent resistance to non-polar fluids such as oils and hydraulic fluids, even at elevated temperatures, and good resistance to the most polar fluids, such as acids, bases, amines and glycols at room temperature. It should be noted that the resistance to polar fluids is poor at temperatures of 70°C or above [54, 55].

Hytrel[®] can be manufactured by different polymer materials for the various applications, such as automotive, electrical/electronic, furniture, appliance and sporting goods. According to the MatWeb technical database, Hytrel[®] has 68 types or grades depending on raw materials, among them, Hytrel[®] RS 40F3 NC010 was chosen for the research. It is a high flow, low modulus grade containing at least 50% renewably sourced ingredients from non-food biomass by its weight, which has excellent low-temperature properties and reduces the environmental impact without compromising performance [54, 56]. Some reported properties of Hytrel[®] RS 40F3 are listed in Table 3.1.

Table 3.1 Property values of Hytrel[®] RS 40F3 NC010.

Properties	Values
Stress at Break	26 MPa
Strain at Break	>300%
Abrasion Resistance	200 mm ³
Melting Temperature	190 °C
Brittleness Temperature	-90 °C
Water Absorption	0.08%
Density	1.11 g/cm ³

Hytrel[®] can be readily formed into high-performance products by different thermoplastic processing techniques, including injection molding, extrusion, blow molding and melt casting. It is processed at temperatures between 180 and 260°C depending on the process and polymer type. Hytrel[®] RS 40F3 was fabricated into nonwoven fabric films through meltblown process from the Nonwovens Institute. Meltblown is a conventional fabrication method of micro- and nanofibers, the thermoplastic polymer melt is extruded through small dies (nozzles) and then it is attenuated to form extremely fine fibers by convergent hot air, these micro- or nanofibers are subsequently blown by high-speed air onto a collector conveyor, thus forming a fine fibered self-bonded meltblown web [57]. Based on the different parameters during meltblown process, there were four samples of Hytrel[®] RS 40F3 films provided by Dr. Shim, shown in Table 3.2.

Table 3.2 Four samples of Hytrel[®] RS 40F3.

Hytrel [®] samples	DCD ^{a)} (mm)	Air (m ³ /hr)	Basic weight (gsm ^{b)})
RS1	150	800	50
RS2	150	1100	50
RS3	150	800	100
RS4	150	1100	100

^{a)} DCD: die-to-collector distance; ^{b)} gsm: grams per square meter (g/m²).

3.2 Experimental Procedure

GO method was used to prepare graphene, involving the synthesis of GO, dispersion in solution and reduction to rGO [58]. GO was prepared according to the modified Hummers method: 230 mL concentrated H₂SO₄ (from Fisher Chemical) was placed into a 6 L Erlenmeyer flask and chilled to 0 °C using an ice bath. Then 6 g graphite powder (from Asbury Graphite

Mills Inc.) was added to the acid and stirred, and 30 g KMnO_4 (from Sigma-Aldrich) was added slowly to prevent the temperature going above 10 °C. After the reaction of the mixture at 35 °C for 2 hours, 460 mL distilled water was added in 20-30 mL aliquots initially. The water addition should be carried out in an ice bath to keep the temperature below 50 °C, because the dilution of sulfuric acid was an exothermic reaction and produced lots of heat. Next, the mixture was stirred for another 2 hours, then 1.4 L distilled (DI) water was added. Shortly after that, 25 mL of 30% H_2O_2 solution (from VWR Analytical) was added to the mixture causing a brilliant yellow color along with bubbling. The mixture was settled for at least a day after which the clear supernatant was decanted. The remaining mixture was washed with 2.5 L of 10% HCl solution (from VWR Analytical) followed by 2.5 L DI water to remove the acid. The resulting GO solution was put through dialysis for 2 weeks to remove remaining metal. Finally, the solid GO could be obtained *via* drying the solution in air at room temperature.

GO was dispersed in the solution to coat Hytrel[®] films. Coating is very suitable for many fiber type substrates, which applied a covering to the surface of a fabric to achieve decorative or functional purposes without significantly altering substrate properties, such as density and flexibility. Due to the extremely low water absorption of 0.08%, Hytrel[®] RS 40F3 was considered to be hydrophobic, and its coating solution should be the organic solvent. N, N-Dimethylformamide (commonly abbreviated as DMF) was used to disperse GO. DMF is an organic compound with the formula $(\text{CH}_3)_2\text{NC}(\text{O})\text{H}$, it is a colorless liquid with the boiling point of 152 °C, which makes it evaporate easier in air compared to NMP (N-Methyl-2-pyrrolidone) with a higher boiling point of 202 °C. The cut Hytrel[®] samples were immersed into 15 mg/mL GO/DMF solution for 10s and then pulled up manually, after the drainage of

excess solution from the surface, the coated samples were placed in glass Petri dishes to evaporate DMF and form the thin GO layer at the surface. Due to the toxicity of DMF, the whole process including dipping and drying should be carried out in a fume hood, moreover, in order to coat film uniformly, the samples needed to be flipped over several times during the drying process. Such dip-coating process could be repeated multiple times to control the GO loading, which was calculated through the GO coated mass divided by the pristine Hytrel[®] weight in the same environment. The more number of coating cycles, the more GO coated on the surface of a sample, thus the better performance of the sensor or supercapacitor could be. However, increased GO loading would also affect stretchiness of the sample, which became worse due to the thicker GO layers on the sample surface. Hence, GO loading should be optimized during the coating process to achieve both good stretchability and sensing activity of the product, which will be discussed below.

There were many methods we mentioned previously to convert GO to graphene, as for the research purpose of sensors and supercapacitors, chemical reduction and laser treatment were applied to remove oxygen-containing functional groups, respectively. For the former, due to the poor resistance of Hytrel[®] to polar fluids at temperatures of 70°C or above, the high concentration hydrazine solution was chosen for the chemical reduction process. Hydrazine, an inorganic compound with the chemical formula N_2H_4 , is a highly effective reducing agent for GO. So, the GO/Hytrel[®] film was immersed in the excessive 50% hydrazine solution for at least a day at room temperature, and the color of the film changed gradually from brown to black, as shown in Figure 3.2. The obtained rGO/Hytrel[®] sample was washed with DI water to remove the hydrazine and then dried in air.

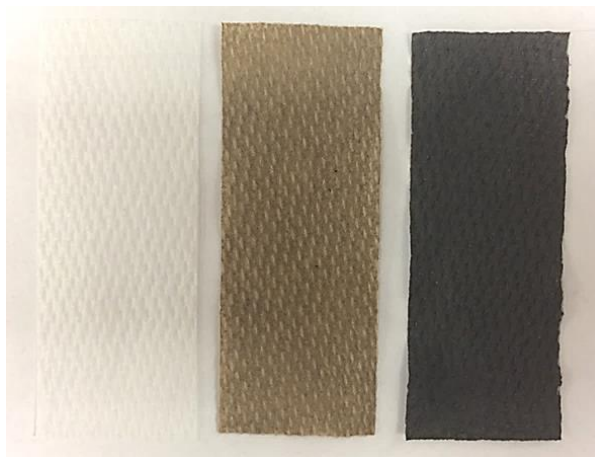


Figure 3.2 Uncoated, coated and reduce GO/Hytrel[®] samples.

For supercapacitors, the GO/Hytrel[®] film was laser treated to transform GO coated on the surface to laser scribed GO (LGO) with different patterns, it was placed on a laser patterning platform (Epilog Mini 18 Laser) equipped with the air-cooled CO₂ laser head. There were two configurations investigated, sandwich and in-plane concentric circular geometries. Typical dimensions of supercapacitors were as follows: sandwich: 8 mm × 8 mm square of LGO on both sides of a 1 cm × 3 cm square of GO/Hytrel[®] film; concentric circular pattern: 3 mm diameter inner circle, 4 mm diameter separating circle, and 5 mm diameter outer circle. The schematics and actual devices of two supercapacitor configurations are shown in Figure 3.3. For the laser patterning, it is more of thermal decomposition, the laser speed and power could be adjusted to control the LGO structure; the higher power and lower speed of the laser would convert GO to more graphitic structures, while it also resulted in the destruction of the Hytrel[®] film when engraving. Therefore, a set of optimized laser processing parameters was important, especially for the sandwich geometrical supercapacitor to avoid circuit shorting.

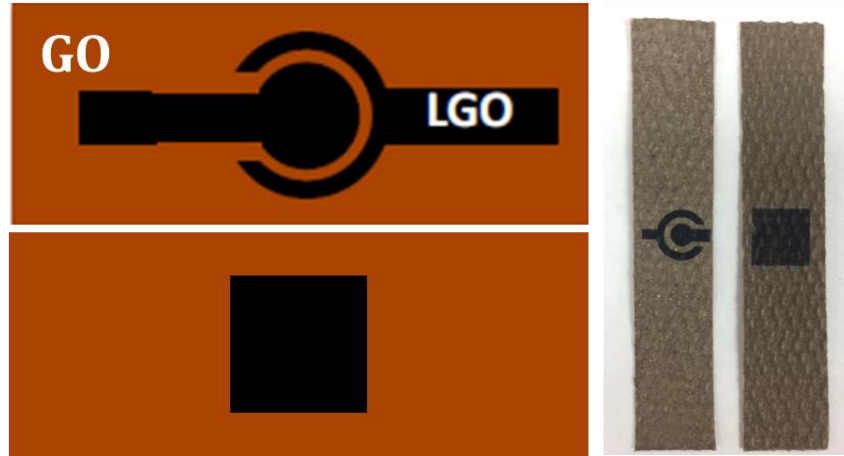


Figure 3.3 The schematics and actual devices of two supercapacitor configurations.

3.3 Characterization Methods

3.3.1 Mechanical Test

Stretch properties test method, ASTM D6614-07, had been used to determine the amount of Hytrel[®] stretch and fabric growth after a specified extension and a specified time [59]. The cut specimen with a dimension of 10 mm × 50 mm was placed in two jaws of MTS Q-test/5 universal testing machine, a constant rate of extension tensile tester. The longer side of the specimen should be parallel to the sides of the jaw faces, and just enough force was applied to remove any folds or wrinkles. A specified load, 0.3 or 0.4 pounds based on different specimens, was applied to the initial Hytrel[®] specimen, the rate of extension was 80 mm/min. After holding at the specified load for 5 minutes, the length was measured. Then the load was removed, after another 5 minutes for the specimen relax, the length was measured again. The amount of fabric stretch is calculated from the difference in length prior to load and under load. Fabric growth is calculated from the difference in length prior to loading and after relaxation.

In addition to stretchiness test, the cycling test was also taken to determine the elastic hysteresis for the uncoated and coated Hytrel[®] films. In a typical measurement, a specimen with the dimension of 10 mm × 50 mm was placed in two jaws of the DIY stretching device, and was stretched manually to different strain values, including 10%, 20%, 30%, 40% and 50% of its original length, for 10 cycles at a constant rate of *ca.* 100 mm/min. After releasing the specimen for 5 min, the length was measured. Since the Hytrel[®] film did not obey Hooke's law perfectly, it would produce a slightly longer length after stretching. The specimens include uncoated Hytrel[®] films and coated ones with different GO loadings, which will be discussed later.

3.3.2 Resistance Test

The Hytrel[®] film with chemically reduced GO was used for strain sensing. The most important parameter measured was the resistance change upon stretching. The specimen with the dimension of 10 mm × 40 mm was placed in two jaws of the DIY stretching device, and its two clamped ends were connected to a digital multimeter (Keysight 34410A) with the conductive copper tape and the silver paste which reduced the contact resistance of the strain sensor. When the specimen was stretched by the DIY stretching device, the resistance increased, which was displayed in the digital multimeter. Such process was depicted in Figure 3.4, and it would be repeated many times to investigate the reproducibility of the resistance-strain relationship.

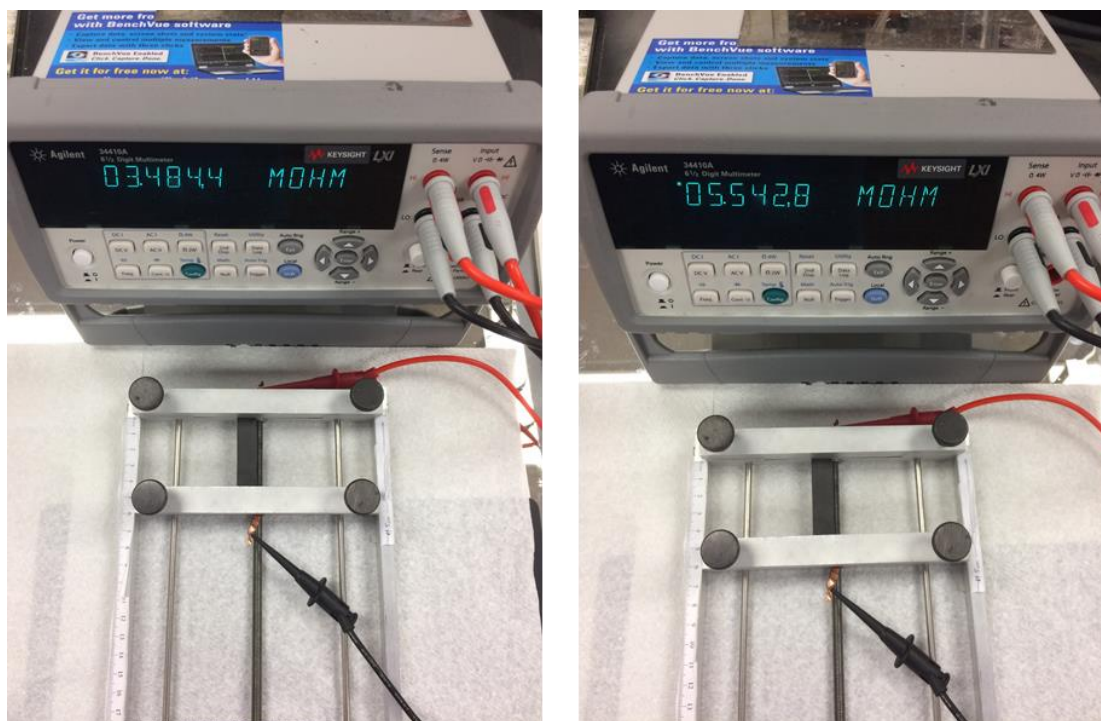


Figure 3.4 Initial resistance and increased resistance upon stretching of the rGO/Hytrel[®] film.

3.3.3 Electrochemical Test

The Hytrel[®] films with LGO were used for supercapacitors. As mentioned previously, the cyclic voltammetry and electrochemical impedance spectroscopy were employed (Metrohm Autolab PGSTAT302N) to characterize the electrochemical performances of supercapacitors. Since two configurations of supercapacitors, including the conventional sandwich and in-plane concentric circular geometries, were prepared, two shape-matching current collectors made of poly vinyl tapes sputter-coated with gold, were also fabricated for collecting electrical signals. The two supercapacitors were shown in Figure 3.5. For the cyclic voltammetry test, the voltage window of 1V was chosen because of the 1 mol/L H₂SO₄-PVA electrolyte employed. Different scan rates were applied in the CV tests to elucidate the rate capability of our devices. Due to the uncertainty in exact mass of the laser-reduced active electrode material, only the areal

capacitance density was reported. For the electrochemical impedance spectroscopy, the most important parameter was the frequency range, and the range of 0.1-10⁶ Hz was employed for our supercapacitors to define the equivalent series resistance (ESR).

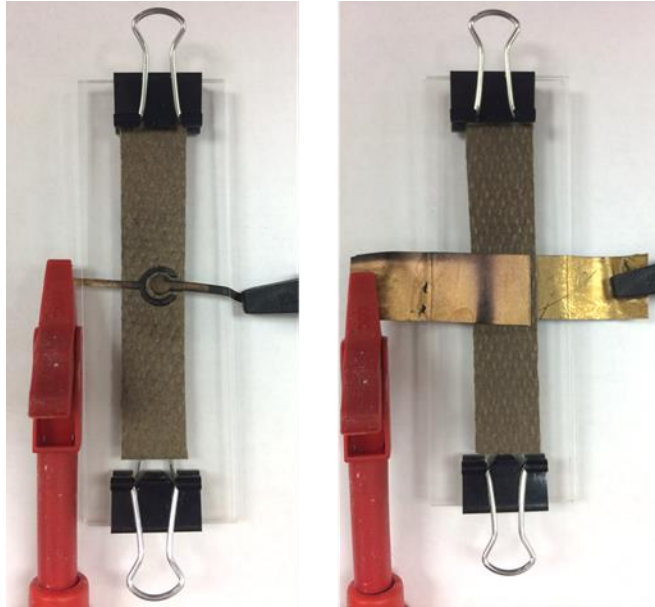


Figure 3.5 Two supercapacitor device assemblies including in-plane and sandwich geometries.

CHAPTER 4 RESULTS AND DISCUSSION

4.1 Mechanical Properties of Hytrel®

4.1.1 Stretchiness

There were four different Hytrel® samples, and they were divided into two groups based on their densities: RS1 and RS2 with 50 gsm, RS3 and RS4 with 100 gsm. Two groups were both tested to identify the Hytrel® films with the best stretchiness for further research, RS1 and RS2 were applied with 0.3 lbs. force load, while RS3 and RS4 were applied with 0.4 lbs. load. Three specimens were tested for each sample, and the final results were presented in Table 4.1.

Table 4.1 Hytrel® stretchiness test data.

Sample	(B-A)/mm	(C-A)/mm
RS1	28.2	2.8
	28.9	2.9
	29.2	3
RS2	21.3	2.2
	19.9	1.9
	21.4	2
RS3	12.3	1.2
	13.4	0.9
	13.6	1.5
RS4	13.3	1.5
	13.9	2.1
	13.1	1.6

where A was the original distance (50 mm) between two jaw faces; B was the distance between jaw faces measured while the specimens under extension force load for 5 min, and C was the

distance between jaw faces measured after removal of force for 5 min. Based on the equation (10) and (11) below:

$$\text{Fabric stretch (\%)} = \frac{B - A}{A} \times 100 \quad (10)$$

$$\text{Fabric growth (\%)} = \frac{C - A}{A} \times 100 \quad (11)$$

The average fabric stretch and fabric growth were calculated and shown in Table 4.2.

Table 4.2 The average fabric stretch and growth of Hytrel®.

Stretch properties	RS1	RS2	RS3	RS4
Fabric stretch (%)	57.5	41.7	26.2	26.9
Fabric growth (%)	5.8	4.1	2.4	3.5

The film thickness has great impact on their applications. While thinner films have higher stretchiness, which is beneficial for strain sensors, they can be easily short circuited for supercapacitors. As shown in Table 4.2, for the thin films (RS1 and RS2) with the thickness of 0.17 mm, RS1 sample had a lower elastic modulus (also named as Young's modulus), since it is stretched longer than RS2 under the same force applied. Thus, RS1 was more sensitive to the stretching force and more suitable for strain sensors. For the thick films (RS3 and RS4) with the thickness of 0.31 mm, the fabric stretch values were similar, but the fabric growth of RS3 was lower than RS4, which meant it had better strain recover property, so RS3 was more suitable for stretchable supercapacitors.

4.1.2 Cycling Property

RS1 and RS3 were chosen for further cycling test. Each sample had three specimens and they were stretched 10 cycles at different strain to determine their fabric growths. The test data was presented in Table 4.3, and the results were shown in Figure 4.1.

Table 4.3 Fabric deformation after stretching 10 cycles at different strain.

strain		10%	20%	30%	40%	50%
Fabric deformation (mm)	RS1	0	0.5	1.2	2	3.1
		0	0.5	1.1	2	2.9
		0	0.5	1.2	2	3
	RS3	0	0.5	1.5	2.5	3.5
		0	0.5	1.5	2.4	3.4
		0	0.5	1.4	2.4	3.5

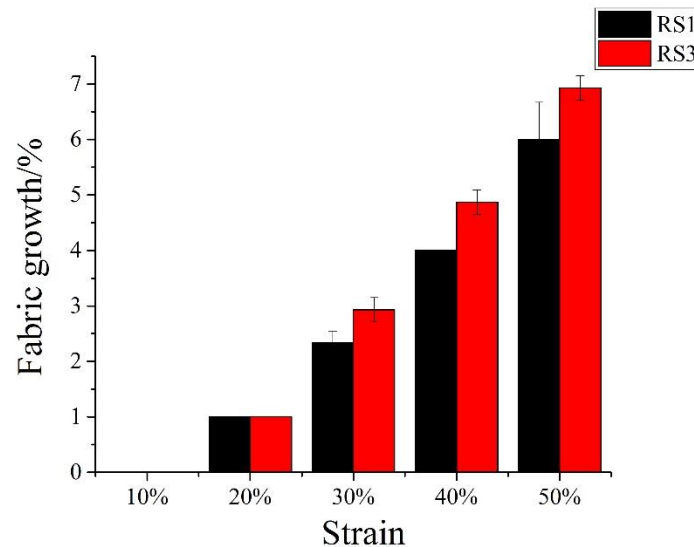


Figure 4.1 The average fabric growth after 10 cycles at different strain.

From the Figure 4.1, the average fabric growths of RS1 and RS3 were both larger than 5% when they were stretched at 50% strain for 10 cycles. So, in order to prevent large permanent

deformation of Hytrel[®] samples, 0 to 40% strain was used for following measurements. Apart from the cycling test for Hytrel[®] RS1 and RS3, the cycling test for coated GO/Hytrel[®] was also carried out to clarify the impact of GO coating on fabric stretchiness. Table 4.4 demonstrated the average fabric growth of coated RS1 sample after 10 cycles at 40% strain. The coated RS1 sample had larger fabric growth or deformation after 10 cycles as compared to the pristine RS1 samples, which implied the cycling property became worse due to the presence of GO in the nonwoven network. At this point, we chose a GO loading of *ca.* $9 \pm 1\%$ to balance between the cyclic stretchiness of Hytrel[®] and electric properties of products.

Table 4.4 The average fabric growth of coated RS1 after 10 cycles at 40% strain.

GO loading	Fabric growth
0%	4%
6%	5%
9%	6%
12%	7%
15%	8%

4.2 Strain Sensor Performances

4.2.1 Resistance Change Under Strain

The rGO/RS1 films were used as strain sensors with the resistance change under strain and gauge factor as important parameters to characterize the performances. Figure 4.2 shows the resistance change and gauge factor dependence on strain (< 10%) for 10 cycles from two samples with *ca.* 10% GO loading. The detail data has been included in Appendices.

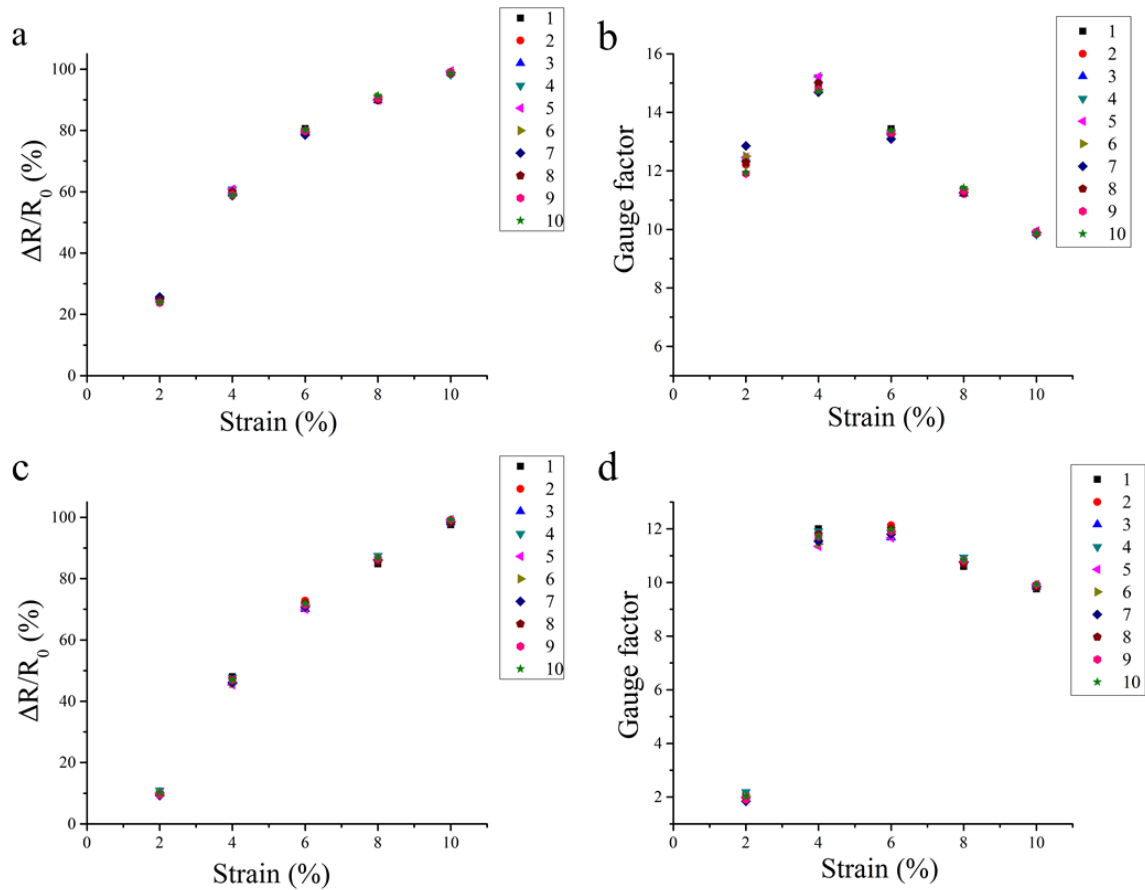


Figure 4.2 The resistance change and gauge factor under low strain for 10 cycles, a & b for sample 1; c & d for sample 2.

When the strain sensor was stretched, the rGO layers coated on the film surface would crack, which limited the electrons transport and caused the resistance increase. In addition to the crack propagation, some graphene sheets might slip and be disconnected from the network during stretching, which also increased the device resistance. From the Figure 4.2, the sample 1 and 2 had the similar $\Delta R/R_0$ vs. strain curves, and both got the highest gauge factors of 15.2 and 12.0, respectively at 4% strain. This stretching process was repeatable with the values of R_0 and ΔR remained the same upon each stretching. Moreover, with the increase in strain, the

gauge factor decreased, and the device became less sensitive to the strain. Interestingly, in Figure 4.3, the resistance change and gauge factor of sample 1 and 2 under high strain (10 ~ 40%) demonstrated the similar trend for 5 cycles, (see the detail data in Appendices).

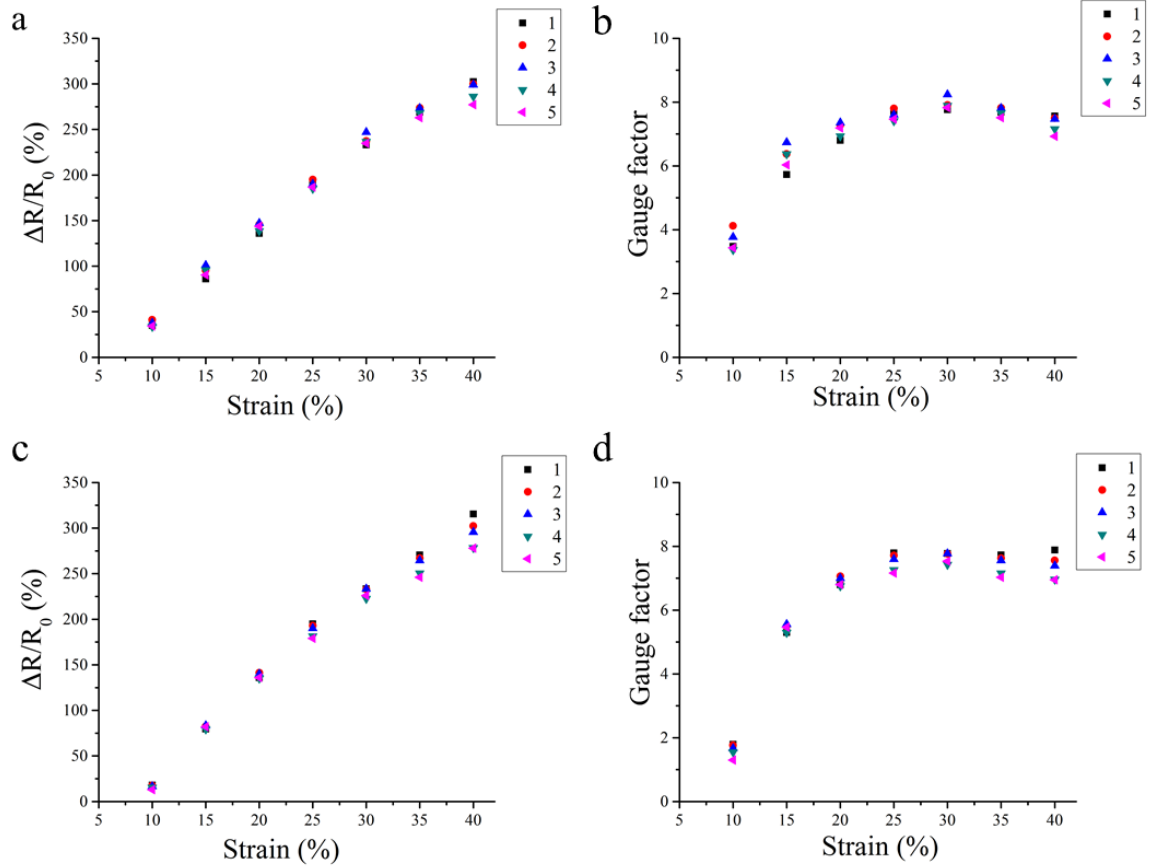


Figure 4.3 The resistance change and gauge factor under high strain for 5 cycles, a & b for sample 1; c & d for sample 2.

As shown in Figure 4.3, sample 1 and 2 had the highest gauge factors of 8.2 and 7.8, respectively at 30% strain, which were both lower than those at 4% strain. The curves of gauge factor became stabilized after 15% strain, although the values of R_0 and ΔR varied during each

stretching, the ratio of R_0 and ΔR almost kept the same. Thus, it can also be used to detect high strain ($>15\%$) with a medium gauge factor.

4.2.2 Heart Rate Detection

In recent years, strain sensors have been evolving rapidly with numerous applications requiring high sensitivity and large strain range. In our case, the strain sensors we made could detect small strain with a relatively high gauge factor, so it was used to measure the heart rate, or the radial pulse from the wrist. The strain sensor film with a dimension of 20×10 mm was contacted closely with the skin of wrist near the radial artery using the double-sided adhesive tape and a moderate pressure, two conductive copper tapes were connected to the two probes of Autolab device. The chrono potentiometry was used to get the voltage curve by applying a constant current of 10^{-5} A. As shown in Figure 4.4, each large sharp peak represents one pulse, and Figure 4.4 (b) was the zoom in region of the red rectangle in Figure 4.4 (a), highlighting a 0.8s pulse including three peaks, P-wave, T-wave and D-wave. Therefore, our strain sensor has demonstrated accurate and reliable detection for heart rate.

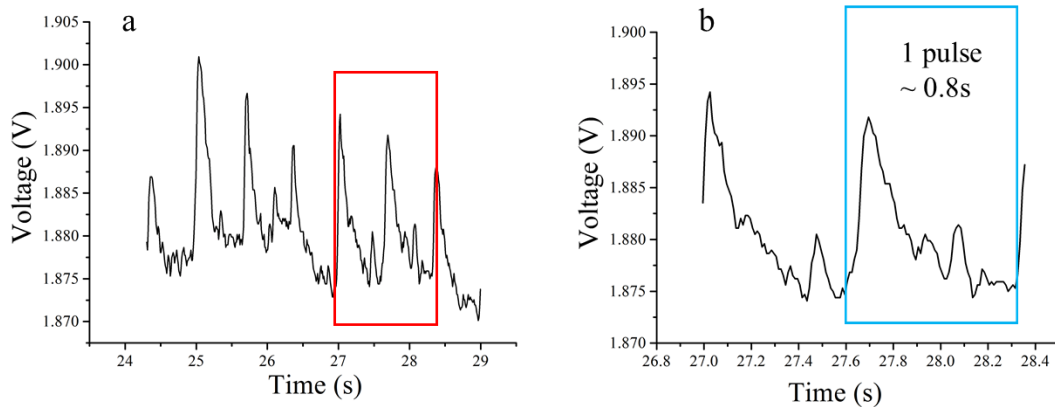


Figure 4.4 The voltage vs. time curve for heart rate detection.

4.2.3 Prototype of Strain Sensor

So far, the strain sensor had been fabricated successfully, however, it needed additional components to integrate into an electronic textile (E-textile) system. An E-textile system should at least include a sensor, a microcontroller board, a power source and a display. Pro Micro board with ATmega32U4 running at 5V/16MHz was chosen due to its low dimensions of 1.3×0.7 ", and the onboard micro-USB connector could be used for powering and programming with cable. The circuit schematic and prototype were presented in Figure 4.5, two resistors in series formed a voltage divider circuit. One end of the resistor pair was hooked up to 5V and the other end was hooked up to ground. The five volts provided by Pro Micro board was divided up between the two resistors, depending on the resistance value of the two resistors. The resistor with the greater resistance got more of the voltage, according to Ohm's law formula:

$$V = I \times R \quad (12)$$

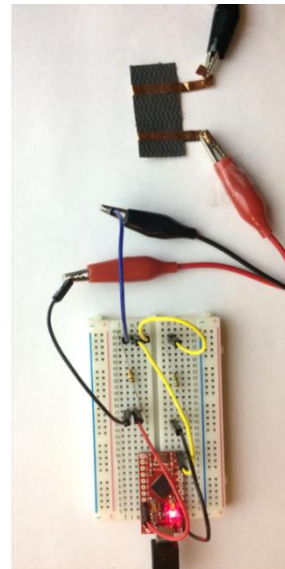
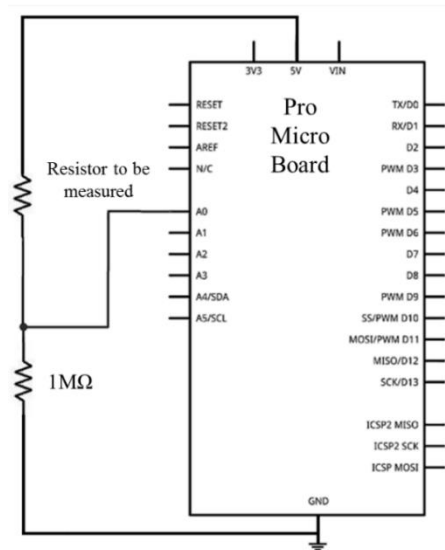


Figure 4.5 The circuit schematic and prototype of strain sensor.

The voltage that fallen across a resistor was directly proportional to its resistance. Using this principle, the code, shown below, was programmed by Arduino to determine the resistance based on the voltage division:

```
const int sensor = A0;

const float VCC = 5; // Measured voltage of 5V line

const float R_DIV = 1; // Measured resistance of 1MΩ resistor

void setup() {

  Serial.begin(9600);

  pinMode(sensor, INPUT);

}

void loop() {

  int reading = analogRead(sensor);

  float RV = reading * VCC / 1023.0;

  float RR = R_DIV * (VCC / RV - 1.0);

  Serial.println(reading); // the result was output into the computer

  Serial.println(RV + " V");

  Serial.println("Resistance: " + String(RR) + " MΩ");

  delay(1000);

}
```

4.3 Supercapacitor Performances

4.3.1 Stretchable Sandwich Supercapacitors

The rGO/RS3 films were used in the supercapacitors for energy storage, for the sandwich geometry, because of the two-sided patterning, the laser of 15% speed and 9% power was selected to avoid shorting. There were two sandwich supercapacitors prepared, S1 with 8.8% GO loading and S2 with 7.6% GO loading. Both were stretchable and can maintain their capacitance within 10% strain, as presented in Table 4.5. The areal capacitance (C_A) were calculated according to the equation (13):

$$C_A = \frac{\int ivdv}{2A\mu\Delta V} \quad (13)$$

where i and v are the current and potential in the CV test (A and V), μ is the scan rate (V/s), A is the area of active materials (cm^2) and ΔV is the potential window. In this case, the integration of i and v was obtained from CV curve shown in Figure 4.6, the scan rate was 0.08 V/s, the area of electrodes was 0.64 cm^2 and the potential window was 1V.

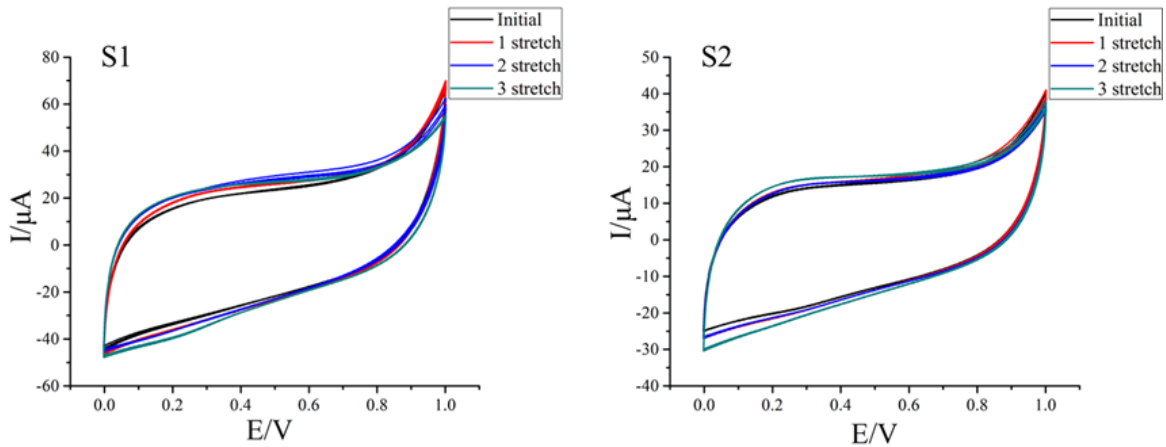


Figure 4.6 The CV curves of supercapacitors S1 and S2.

Table 4.5 The areal capacitance and its change upon stretching.

Sandwich supercapacitors	C_A (mF/cm ²)	C_A change	
S1	Initial capacitance	1.533	
	After 1 stretching	1.635	6.60%
	After 2 stretching	1.649	0.85%
	After 3 stretching	1.647	-0.09%
S2	Initial capacitance	1.049	
	After 1 stretching	0.994	-5.25%
	After 2 stretching	1.004	1.06%
	After 3 stretching	0.973	-3.16%

In Table 4.5, the first stretching within its elasticity had caused capacitance change (+/-). This might result from some physical changes in supercapacitors, for example, graphene layer structures of electrodes might change during the first stretching, or electrolyte diffused into electrodes, *etc.* These changes led to the increase or decrease of the capacitance, however, in the next stretching cycles, the capacitance basically remained the same. The supercapacitor S3 with 9% GO loading had confirmed this conclusion, as shown in Table 4.6 and Figure 4.7, where it had been stretched for 12 cycles at 10% strain, and its capacitance almost kept the same after the first stretching. Its CV curves with different scan rates were presented in Figure 4.8, as the increase of the scan rate, the CV curve shape became more like a rectangle, which implied the supercapacitor S3 had the high rate capability.

Table 4.6 The areal capacitance and its change of the supercapacitor S3.

Cycles	C_A (mF/cm ²)	C_A change
0	1.676	
1	1.501	-10.43%
2	1.578	5.11%
3	1.559	-1.22%
4	1.524	-2.26%
5	1.503	-1.33%
6	1.453	-3.35%
7	1.497	3.05%
8	1.455	-2.85%
9	1.506	3.50%
10	1.508	0.18%
11	1.465	-2.85%
12	1.468	0.23%

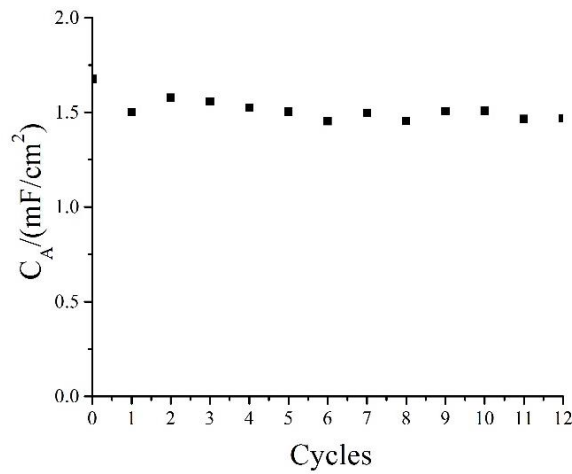


Figure 4.7 The area-specific capacitance of S3 during stretching cycles.

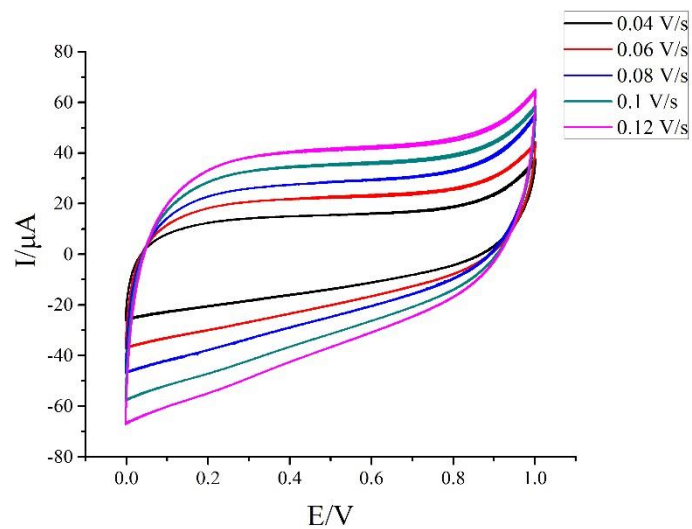


Figure 4.8 The CV curves of S3 with different scan rates.

In order to calculate the energy density and power density based on the equations (8) and (9), the equivalent series resistance (ESR) is needed, which is defined by the intersection of the Nyquist curve with the X-axis in EIS. The Nyquist plots of S1 and S2 were shown in Figure 4.9, with the steeper lines observed at low-frequency region after stretching, which suggested the better electrolyte diffusion in the electrodes.

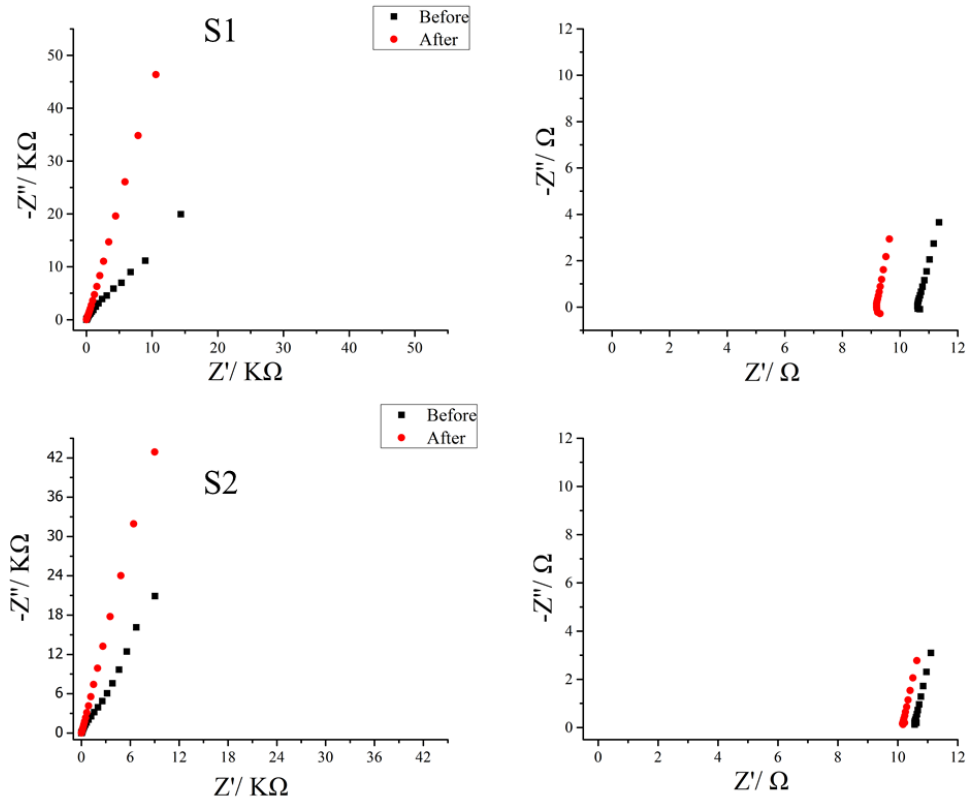


Figure 4.9 Nyquist plots of supercapacitor S1& S2. (Right insets) Zoom-in images of the high-frequency regime.

4.3.2 In-plane Concentric Circular Supercapacitors

Supercapacitors with in-plane concentric circular geometry were not stretchable, since the current collects needed to fit the electrode area very well in this configuration, and a little deformation after stretching would cause the bad contact between them, resulting in large capacitance change. The laser of 15% speed and 10% power was selected due to the one-sided patterning, and a higher laser power can convert GO to more graphitic structures, leading to a higher capacitance. The areal capacitance of three supercapacitors with the area of 0.2 cm^2 was listed in Table 4.7.

Table 4.7 The areal capacitance of supercapacitor C1, C2 & C3.

In-plane supercapacitors	GO loading (%)	C_A (mF/cm ²)
C1	9.2	0.781
C2	8.5	0.631
C3	8.8	0.7

The areal capacitance of the in-plane concentric circular supercapacitor was much lower than that of the sandwich supercapacitor, since only one electrode area was counted in the sandwich supercapacitors when calculating the capacitance, while for the in-plane concentric circular supercapacitor, the value was based on the sum of both electrode areas. The CV and Nyquist plots of in-plane concentric circular supercapacitors are shown in Figure 4.10 with the scan rate of 80 mV/s. The rectangular CV curves were beneficial for supercapacitors, and the steep lines in Nyquist plots suggested a good electrolyte diffusion in the electrodes, however, the equivalent series resistance was much higher, which was *ca.* 120 Ω . It might result from the contact resistance between the current collector and the electrode, and would affect the power density of the in-plane supercapacitor.

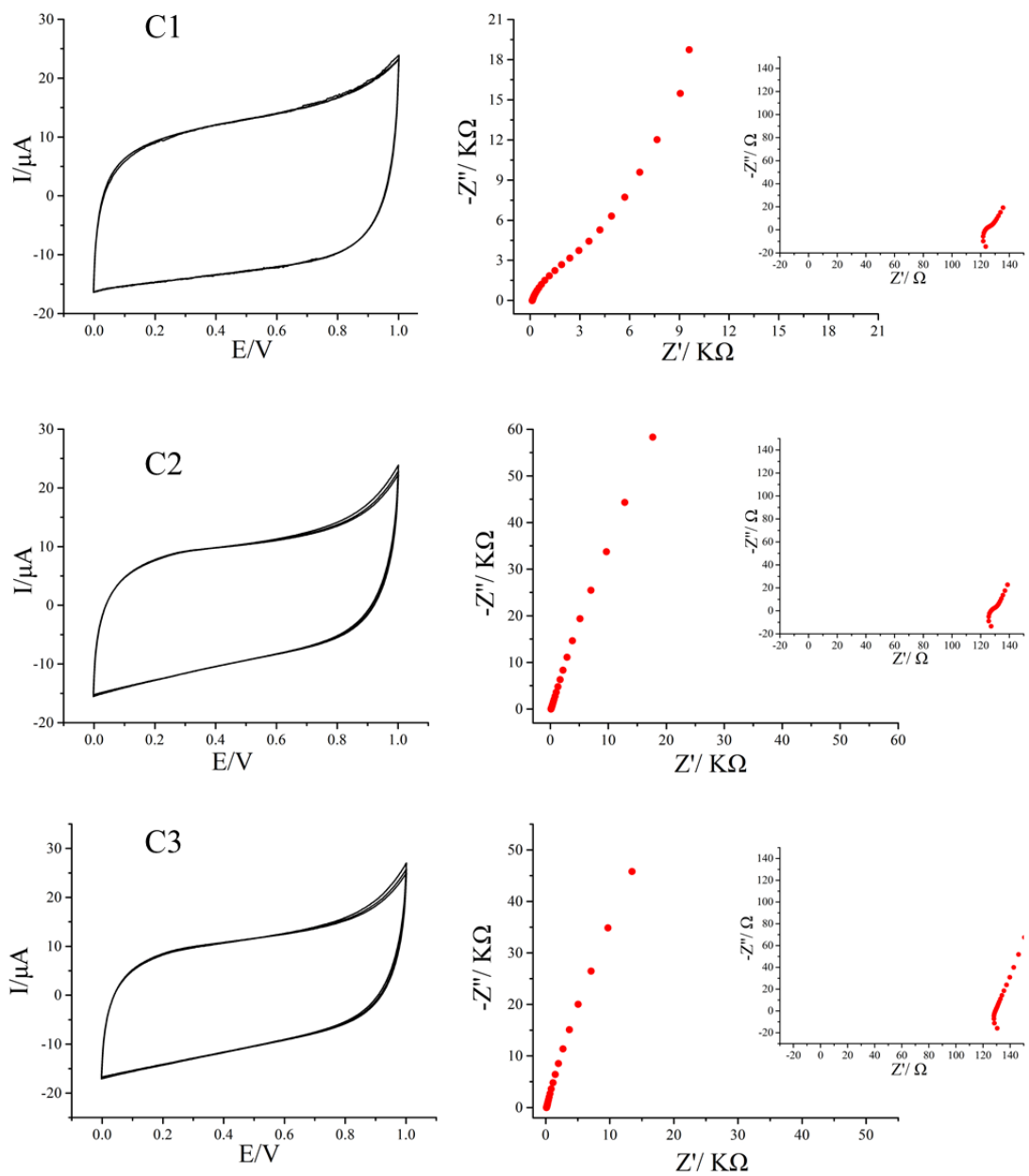


Figure 4.10 The CV and Nyquist plots of supercapacitor C1, C2 & C3, the same sample of each row. (Right insets) Zoom-in images of the high-frequency regime of Nyquist plots.

CHAPTER 5 CONCLUSIONS AND FUTURE WORK

5.1 Conclusions

The graphene coated Hytrel[®] films were used as wearable electronics for sensing and energy storage. Two types of Hytrel[®] RS 40F3 films were selected based on their mechanical properties. RS1 film was used in the strain sensor *via* dip coating and chemical reduction of GO, and it could detect low strain (<10%) with a gauge factor of 15.2 and high strain (15 to 40%) with a gauge factor of 8.2. In comparison to other strain sensors, our graphene/Hytrel[®] RS1 strain sensor has a medium strain range and gauge factor; however, its production process was simple and low-cost. In addition, the Hytrel[®] films are nonwoven fabrics that are highly breathable and can interact favorably with human body. Thus, our strain sensors made of graphene and Hytrel[®] RS1 films can be easily integrated into wearable devices for various applications, such as motion detection, and heart rate measurement from radial artery of the wrist.

For graphene-based supercapacitors, Hytrel[®] RS3 film was chosen as the substrate for supercapacitors through dip coating and laser patterning process. Two configurations of supercapacitors have been employed: the sandwich and in-plane concentric circular geometries. With similar GO loadings, the sandwich supercapacitors were stretchable with a stable areal capacitance of $\sim 1.6 \text{ mF/cm}^2$ upon 10% strain and a very small equivalent series resistance of $\sim 10 \Omega$. The in-plane supercapacitors are not stretchable in our experiments mainly due to the limited affinity between the current collectors and in-plane electrodes. Their areal capacitance could reach 0.78 mF/cm^2 with a relatively high equivalent series resistance of $\sim 120 \Omega$. These

two types of supercapacitors involving graphene and Hytrel[®] RS3 films can also be used in wearable devices for energy storage.

5.2 Future Work

For the strain sensor, its strain responsive mechanism needs to be clarified. In addition, the fabrication process of strain sensor can be improved to obtain better performances, for instance, we can control the size of the graphene sheet during the GO preparation to see its effect on the conductivity, and we can also dope carbon nanotube into the GO coating solution to achieve a higher conductivity. As for the chemical reduction, we can try different reducing agents or the vapor reduction method to reduce GO more effectively. The strain sensor we made can be used in many applications that require high sensitivity or large strain range, thus, apart from the heart rate detection, we will try more applications, e.g. the sound detection from throat, respiration rate, and the movement detection of the finger or knee.

For the supercapacitor part, we can attempt more geometries of electrodes, such as parallel column and hairbrush patterns. Since graphene-based supercapacitors are electrochemical double-layer capacitors that have the lower capacitance, we can incorporate redox materials to increase it, such as ruthenium oxide (RuO_2), the most promising electrode material due to its high specific capacitance (720 F/g). Furthermore, the supercapacitors can absorb energy generated by the triboelectric nanogenerators that were made from the Hytrel[®] and aluminum film, since they have different abilities to attract electrons, a charge transfer of surface will occur when they are brought into contact [59]. Finally, when supercapacitors reach a high enough energy density, they can be used in energy sources for the strain sensor to achieve a complete product combination.

REFERENCES

- [1] Boland, Conor S., et al. "Sensitive electromechanical sensors using viscoelastic graphene-polymer nanocomposites." *Science* 354.6317 (2016): 1257-1260.
- [2] Li, Xiao, et al. "Stretchable and highly sensitive graphene-on-polymer strain sensors." *Scientific reports* 2 (2012): 870.
- [3] Yan, Chaoyi, et al. "Highly stretchable piezoresistive graphene-nanocellulose nanopaper for strain sensors." *Advanced materials* 26.13 (2014): 2022-2027.
- [4] Niu, Zhiqiang, et al. "Highly Stretchable, Integrated Supercapacitors Based on Single-Walled Carbon Nanotube Films with Continuous Reticulate Architecture." *Advanced Materials* 25.7 (2013): 1058-1064.
- [5] Hu, Liangbing, et al. "Stretchable, porous, and conductive energy textiles." *Nano letters* 10.2 (2010): 708-714.
- [6] Soldano, Caterina, Ather Mahmood, and Erik Dujardin. "Production, properties and potential of graphene." *Carbon* 48.8 (2010): 2127-2150.
- [7] Singh, Virendra, et al. "Graphene based materials: past, present and future." *Progress in materials science* 56.8 (2011): 1178-1271.
- [8] Kuila, Tapas, et al. "Chemical functionalization of graphene and its applications." *Progress in Materials Science* 57.7 (2012): 1061-1105.
- [9] Wallace, Philip Richard. "The band theory of graphite." *Physical Review* 71.9 (1947): 622.
- [10] Novoselov, Kostya S., et al. "Electric field effect in atomically thin carbon films." *science* 306.5696 (2004): 666-669.

- [11] Geim, Andre K., and Konstantin S. Novoselov. "The rise of graphene." *Nature materials* 6.3 (2007): 183-191.
- [12] Choi, Wonbong, and Jo-won Lee, eds. *Graphene: synthesis and applications*. CRC Press, 2011.
- [13] Novoselov, Konstantin S., et al. "A roadmap for graphene." *Nature* 490.7419 (2012): 192-200.
- [14] El-Kady, Maher F., Yuanlong Shao, and Richard B. Kaner. "Graphene for batteries, supercapacitors and beyond." *Nature Reviews Materials* 1 (2016): 16033.
- [15] Compton, Owen C., and SonBinh T. Nguyen. "Graphene oxide, highly reduced graphene oxide, and graphene: versatile building blocks for carbon - based materials." *small* 6.6 (2010): 711-723.
- [16] Lerf, Anton, et al. "Structure of graphite oxide revisited." *The Journal of Physical Chemistry B* 102.23 (1998): 4477-4482.
- [17] He, Heyong, et al. "A new structural model for graphite oxide." *Chemical physics letters* 287.1 (1998): 53-56.
- [18] Pei, Songfeng, and Hui-Ming Cheng. "The reduction of graphene oxide." *Carbon* 50.9 (2012): 3210-3228.
- [19] Park, Sungjin, and Rodney S. Ruoff. "Chemical methods for the production of graphenes." *Nature nanotechnology* 4.4 (2009): 217-224.
- [20] Zhou, Yong, et al. "Hydrothermal dehydration for the "green" reduction of exfoliated graphene oxide to graphene and demonstration of tunable optical limiting properties." *Chemistry of Materials* 21.13 (2009): 2950-2956.

- [21] Ramesha, Ganganahalli K., and Srinivasan Sampath. "Electrochemical reduction of oriented graphene oxide films: an in situ Raman spectroelectrochemical study." *The Journal of Physical Chemistry C* 113.19 (2009): 7985-7989.
- [22] Williams, Graeme, Brian Seger, and Prashant V. Kamat. "TiO₂-graphene nanocomposites. UV-assisted photocatalytic reduction of graphene oxide." *ACS nano* 2.7 (2008): 1487-1491.
- [23] Gao, Wei, et al. "New insights into the structure and reduction of graphite oxide." *Nature chemistry* 1.5 (2009): 403-408.
- [24] Brownson, Dale AC, and Craig E. Banks. *The handbook of graphene electrochemistry*. London: Springer, 2014.
- [25] Bolotin, Kirill I., et al. "Ultrahigh electron mobility in suspended graphene." *Solid State Communications* 146.9 (2008): 351-355.
- [26] Li, Dan, et al. "Processable aqueous dispersions of graphene nanosheets." *Nature nanotechnology* 3.2 (2008): 101-105.
- [27] Pantelopoulos, Alexandros, and Nikolaos G. Bourbakis. "A survey on wearable sensor-based systems for health monitoring and prognosis." *IEEE Transactions on Systems, Man, and Cybernetics, Part C (Applications and Reviews)* 40.1 (2010): 1-12.
- [28] Mukhopadhyay, Subhas Chandra. "Wearable sensors for human activity monitoring: A review." *IEEE sensors journal* 15.3 (2015): 1321-1330.
- [29] Patel, Shyamal, et al. "A review of wearable sensors and systems with application in rehabilitation." *Journal of neuroengineering and rehabilitation* 9.1 (2012): 21.
- [30] de Rossi, Danilo Emilio, and Rita Paradiso. "Future direction: e-textiles." *Wearable*

Monitoring Systems. Springer US, 2011. 147-162.

[31] Hoffmann, Karl. "An introduction to stress analysis and transducer design using strain gauges." *HBM Test and Measurement* (2012).

[32] Jamshidi, Babak, and Albert P. Pisano. "Capacitive strain sensor." U.S. Patent No. 8,342,031. 1 Jan. 2013.

[33] Chen, Peter C., and Shiping Chen. "Fiber optic strain sensor." U.S. Patent No. 6,668,105. 23 Dec. 2003.

[34] Amjadi, Morteza, et al. "Highly stretchable and sensitive strain sensor based on silver nanowire–elastomer nanocomposite." *ACS nano* 8.5 (2014): 5154-5163.

[35] Yamada, Takeo, et al. "A stretchable carbon nanotube strain sensor for human-motion detection." *Nature nanotechnology* 6.5 (2011): 296-301.

[36] Amjadi, Morteza, et al. "Stretchable, Skin-Mountable, and Wearable Strain Sensors and Their Potential Applications: A Review." *Advanced Functional Materials* (2016).

[37] Castano, Lina M., and Alison B. Flatau. "Smart fabric sensors and e-textile technologies: a review." *Smart Materials and Structures* 23.5 (2014): 053001.

[38] Lu, Nanshu, et al. "Highly sensitive skin - mountable strain gauges based entirely on elastomers." *Advanced Functional Materials* 22.19 (2012): 4044-4050.

[39] Wang, Dan-Yang, et al. "High performance flexible strain sensor based on self-locked overlapping graphene sheets." *Nanoscale* 8.48 (2016): 20090-20095.

[40] Wang, Yan, et al. "Wearable and highly sensitive graphene strain sensors for human motion monitoring." *Advanced Functional Materials* 24.29 (2014): 4666-4670.

[41] Simmons, John G. "Generalized formula for the electric tunnel effect between similar

electrodes separated by a thin insulating film." *Journal of applied physics* 34.6 (1963): 1793-1803.

[42] Burke, Andrew. "Ultracapacitors: why, how, and where is the technology." *Journal of power sources* 91.1 (2000): 37-50.

[43] Zhang, Yong, et al. "Progress of electrochemical capacitor electrode materials: A review." *International journal of hydrogen energy* 34.11 (2009): 4889-4899.

[44] Wang, Guoping, Lei Zhang, and Jiujun Zhang. "A review of electrode materials for electrochemical supercapacitors." *Chemical Society Reviews* 41.2 (2012): 797-828.

[45] Zhang, Li Li, and X. S. Zhao. "Carbon-based materials as supercapacitor electrodes." *Chemical Society Reviews* 38.9 (2009): 2520-2531.

[46] Xiong, Guoping, et al. "A review of graphene-based electrochemical microsupercapacitors." *Electroanalysis* 26.1 (2014): 30-51.

[47] Jost, Kristy, Genevieve Dion, and Yury Gogotsi. "Textile energy storage in perspective." *Journal of Materials Chemistry A* 2.28 (2014): 10776-10787.

[48] Zhi, Mingjia, et al. "Nanostructured carbon-metal oxide composite electrodes for supercapacitors: a review." *Nanoscale* 5.1 (2013): 72-88.

[49] Conway, Brian E. *Electrochemical supercapacitors: scientific fundamentals and technological applications*. Springer Science & Business Media, 2013.

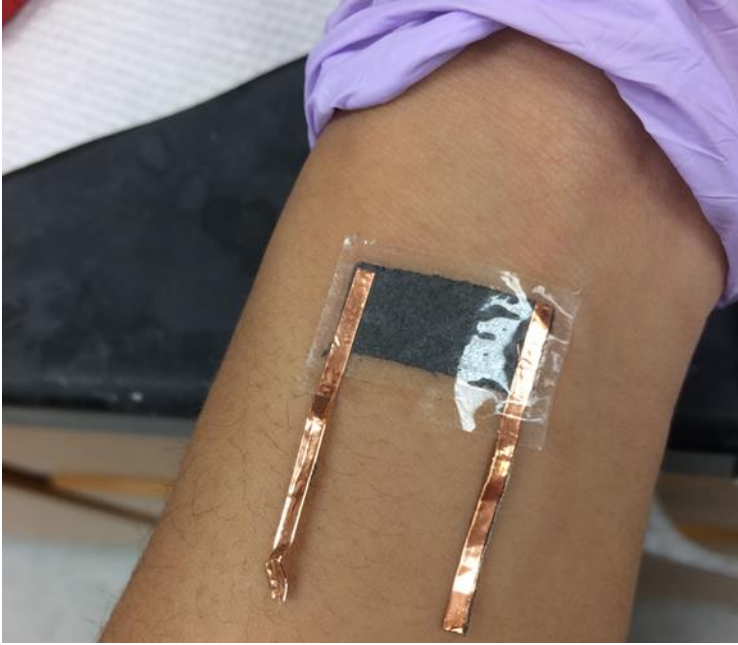
[50] Augustyn, Veronica, Patrice Simon, and Bruce Dunn. "Pseudocapacitive oxide materials for high-rate electrochemical energy storage." *Energy & Environmental Science* 7.5 (2014): 1597-1614.

[51] Zhang, Li Li, Rui Zhou, and X. S. Zhao. "Graphene-based materials as supercapacitor

- electrodes." *Journal of Materials Chemistry* 20.29 (2010): 5983-5992.
- [52] Stoller, Meryl D., et al. "Graphene-based ultracapacitors." *Nano letters* 8.10 (2008): 3498-3502.
- [53] "DUPONT™ HYTREL® THERMOPLASTIC POLYESTER ELASTOMER PRODUCT REFERENCE GUIDE." Web.
- [54] "DUPONT™ HYTREL® Design Guide." Web.
- [55] "DUPONT™ HYTREL® Fluid and Chemical Resistance Guide." Web.
- [56] "Hytrel® Technical Data Sheets." *MatWeb*. N.p., n.d. Web
- [57] Horrocks, A. Richard, and Subhash C. Anand, eds. *Handbook of technical textiles*. Elsevier, 2000.
- [58] Gilje, Scott, et al. "A chemical route to graphene for device applications." *Nano letters* 7.11 (2007): 3394-3398.
- [59] Yi, Fang, et al. "Stretchable - Rubber - Based Triboelectric Nanogenerator and Its Application as Self - Powered Body Motion Sensors." *Advanced Functional Materials* 25.24 (2015): 3688-3696.

APPENDICES

The assembly of strain sensor for heart rate detection (page 38)



The tables of Sample 1 test data (page 36, 37)

Strain (%)	Resistance change for 10 cycles (%)									
2	24.63	24.41	24.78	24.56	24.93	25.00	25.71	24.57	23.81	23.89
4	59.82	59.12	60.35	60.82	60.87	59.09	58.76	60.00	59.10	58.89
6	80.65	79.41	79.88	79.82	79.71	79.55	78.53	79.71	79.83	80.28
8	90.62	89.71	89.80	90.64	89.86	90.91	90.11	90.00	90.48	91.39
10	98.83	98.53	98.83	98.25	99.42	98.86	98.87	98.57	98.88	98.61

Strain (%)	Gauge factor for 10 cycles									
2	12.32	12.21	12.39	12.28	12.46	12.50	12.85	12.29	11.90	11.94

4	14.96	14.78	15.09	15.20	15.22	14.77	14.69	15.00	14.78	14.72
6	13.44	13.24	13.31	13.30	13.29	13.26	13.09	13.29	13.31	13.38
8	11.33	11.21	11.22	11.33	11.23	11.36	11.26	11.25	11.31	11.42
10	9.88	9.85	9.88	9.82	9.94	9.89	9.89	9.86	9.89	9.86

Strain (%)	Resistance change for 5 cycles (%)				
10	34.76	41.21	37.70	33.66	34.29
15	85.98	95.60	101.05	95.54	90.48
20	135.98	145.60	147.12	138.61	143.81
25	192.68	195.05	190.05	185.15	186.67
30	232.93	237.36	247.12	236.63	234.76
35	268.90	273.63	273.30	267.82	262.86
40	302.44	300.00	298.95	286.14	277.14

Strain (%)	Gauge factor for 5 cycles				
10	3.48	4.12	3.77	3.37	3.43
15	5.73	6.37	6.74	6.37	6.03
20	6.80	7.28	7.36	6.93	7.19
25	7.71	7.80	7.60	7.41	7.47
30	7.76	7.91	8.24	7.89	7.83
35	7.68	7.82	7.81	7.65	7.51
40	7.56	7.50	7.47	7.15	6.93

The tables of Sample 2 test data (page 36, 37)

Strain (%)	Resistance change for 10 cycles (%)									
2	10.40	9.60	10.24	10.94	10.00	10.08	9.23	9.60	9.52	10.16
4	48.00	46.40	46.46	47.66	45.38	45.74	46.15	47.20	46.83	46.88
6	72.00	72.80	70.08	71.09	70.00	71.32	70.77	72.00	71.43	71.88
8	84.80	85.60	86.61	87.50	86.15	86.05	86.15	85.60	86.51	86.72
10	97.60	98.40	98.43	98.44	99.23	98.45	98.46	98.40	99.21	99.22

Strain (%)	Gauge factor for 10 cycles									
2	2.08	1.92	2.05	2.19	2.00	2.02	1.85	1.92	1.90	2.03
4	12.00	11.60	11.61	11.91	11.35	11.43	11.54	11.80	11.71	11.72
6	12.00	12.13	11.68	11.85	11.67	11.89	11.79	12.00	11.90	11.98
8	10.60	10.70	10.83	10.94	10.77	10.76	10.77	10.70	10.81	10.84
10	9.76	9.84	9.84	9.84	9.92	9.84	9.85	9.84	9.92	9.92

Strain (%)	Resistance change for 5 cycles (%)				
10	17.95	17.65	16.67	15.46	13.00
20	135.90	141.18	140.00	135.05	82.00
25	194.87	192.94	190.00	181.44	136.00
30	233.33	232.94	233.33	222.68	179.00
35	270.51	267.06	264.44	250.52	226.00
40	315.38	302.35	295.56	278.35	246.00

Strain (%)	Gauge factor for 5 cycles				
10	1.79	1.76	1.67	1.55	1.30
15	5.30	5.49	5.56	5.29	5.47
20	6.79	7.06	7.00	6.75	6.80
25	7.79	7.72	7.60	7.26	7.16
30	7.78	7.76	7.78	7.42	7.53
35	7.73	7.63	7.56	7.16	7.03
40	7.88	7.56	7.39	6.96	6.95